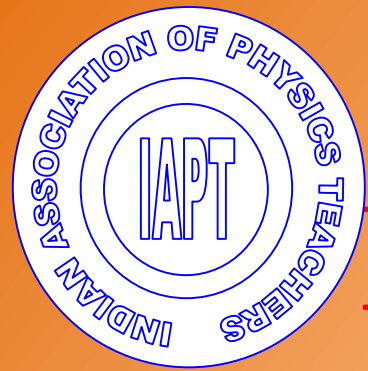
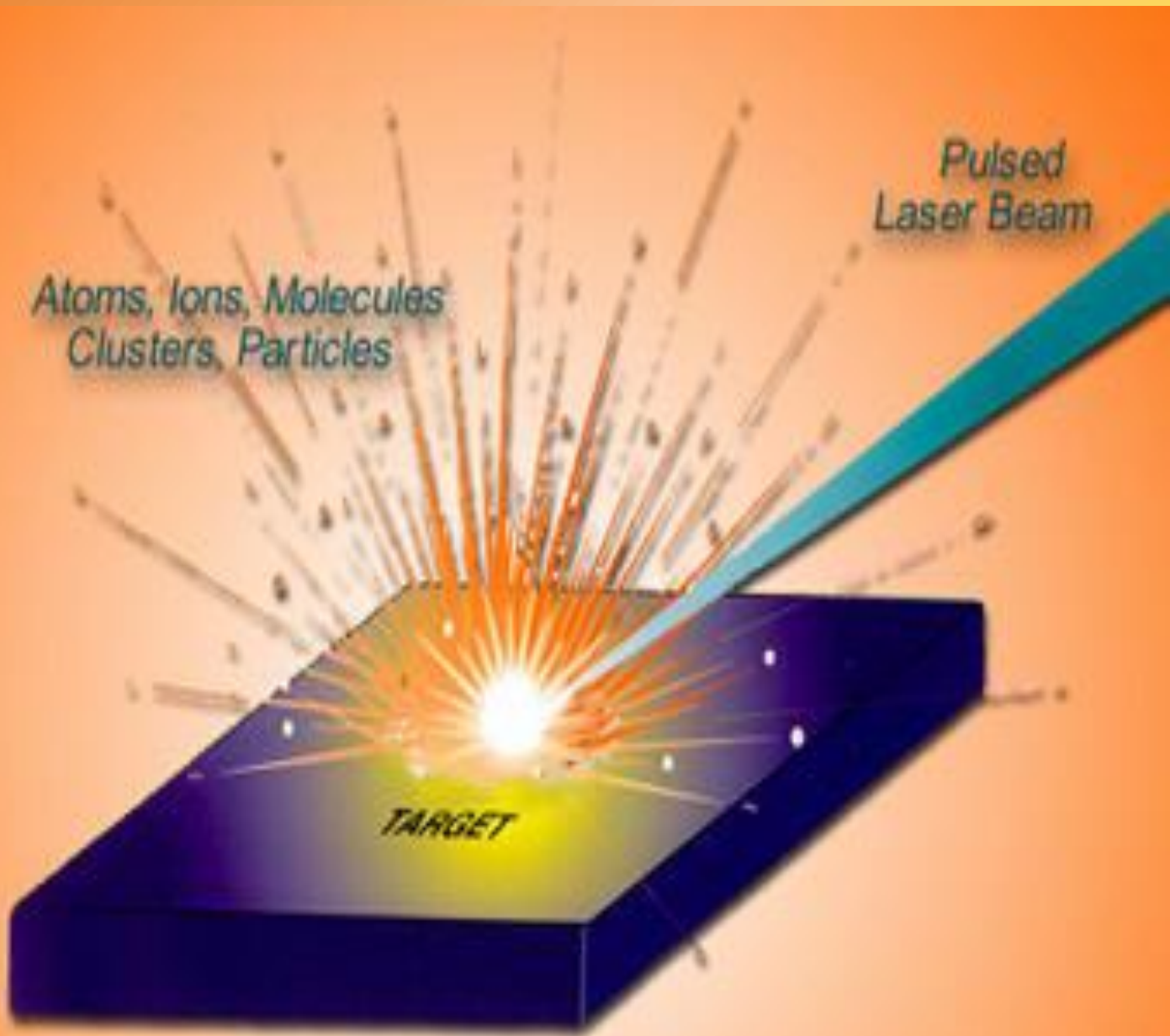


Vol 33 No. 4 Oct - Dec 2017 ISSN 0970-5953



PHYSICS EDUCATION



Volume 33, Number 4**In this Issue**

- **Demonstration of Dielectric Breakdown of Air Using Electronic Waste** 04 Pages
Kamlesh Alti
- **Laser Zap: An Optical Approach for Elemental Analysis of Sample Surfaces** 05 Pages
Zeenab A. Pathan, Raja V. L. N, Sridhar, S. B. Patil, Adwaita Goswami, Kalpana Aravind and
Laxmiprasad A.S.
- **Exploration of the Quantum Casimir Effect** 07 Pages
Antonius Torode
- **Rheology in the Teaching Lab: Properties of Starch Suspensions** 13 Pages
J. A. Groman, J. I. Katz and J. G. Miller
- **Sum Rules in Non-relativistic Quantum Mechanics** 10 Pages
Debnarayan Jana

Demonstration of Dielectric Breakdown of Air Using Electronic Waste

Kamlesh Alti

Department of Physics
Sant Gadge Baba Amravati University
Amravati 444602, India.

Submitted on 23-11-2017

Abstract

Student generally observe dielectric breakdown of air during thunderstorm in the form of cloud to cloud and cloud to ground lightning bolts. Same can be realized in the classroom or laboratory experiment with the help of electronic waste of old cathode ray tube TV set. This paper demonstrates the usefulness of electronic waste to demonstrate multiple physics concepts to secondary and higher secondary students.

1. Introduction

Occurrence of lightning during stormy weather is very common. In fact such weather condition inspired Benjamin Franklin to perform his famous kite experiment in 1752 [1]. This experiment proves that the thunderclouds are electrified and lightning is just an electrical discharge. In 1906 Russell Alexander reported experiments for measurement of dielectric strength of air which was found to be around 38 kV/cm [2]. Many experiments were conducted after that for confirming the dielectric strength of 30 kV/cm [3]. Sphere gap method is one of the established

2. Experimental Set up and Results

An old CRT TV set with remote was procured from the market at a very cheap price. Before making

standard method for measuring air breakdown and electric field [4]. Under normal temperature and pressure condition the current conduction in atmospheric gases is approximately equal to 10^{-10} A/cm² which may be because of generation of minuscule amount of ionized air due to interaction with cosmic radiation and radioactive substances. Classroom demonstration of dielectric breakdown of air is a challenge in itself as it require the need of high voltages and corresponding safety issues. Students especially secondary and higher secondary are found to be curious about the shape, size and color of electric discharge. Moreover, types of matter is a part of curricula of secondary school education. They learn, Plasma as the fourth state of matter in this part. During the air breakdown plasma is forming for a very short duration ranging in few nanoseconds which substantially increase electrical conductivity. Classroom demonstration of this increase in the electrical conductivity is possible if we could successfully shows the dielectric breakdown of air. Hence in this paper, we demonstrate dielectric air breakdown using electronically waste product i.e. an old cathod ray tube (CRT) television (TV) set.

purchase, we have ensured that the high voltage (HV) plate connected to CRT is intact and in working condition. This particular HV plate was giving output of 18 kV. After procuring, HV plate was taken off the set carefully. Fig. 1 shows the image HV plate. Details of the construction and working of TV plate is as follows. In the colour T.V plate different sections

are present viz; Video section, Audio section, power supply section etc. Out of these sections only power supply section is used here. Housing for the HV plate was created using old wooden boxes laying idle in the institute. The entire set up with housing is as shown in Fig. 2. HV plate was mounted inside of the wooden box having one small glass window for smooth working of remote operation. Positive output of the

HV plate was connected to sewing needle electrode mounted on the top of the wooden box. Tip of the needle used as an electrode has diameter of 0.6 mm. Receiving needle electrode having same dimension was also mounted opposite to first one. Receiving electrode was grounded appropriately by constructing in-house earthing using charcoal, salt and soil as shown in the bottom inset of Fig. 2.

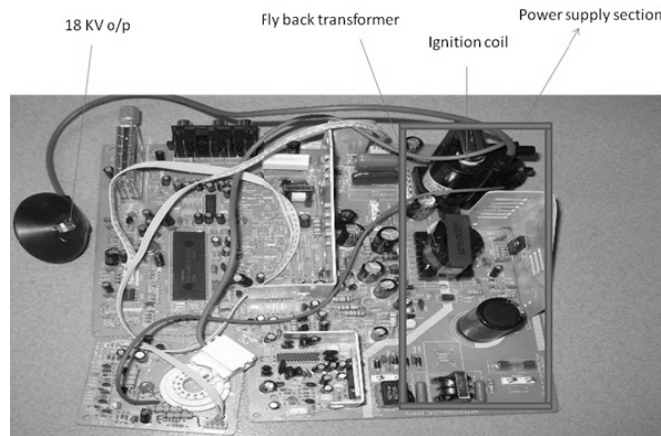


Fig.1: Image of the High Voltage plate of Television.



Fig. 2: Electric arc generation set up using electronic waste.
Inset picture shows constructed ground for receiving electrode.

Upon providing electric supply to the HV plate and switching it ON with the help of remote, electric arc was seen as shown in Fig. 3. Leak current was detected for different distances between the needle

electrodes by connecting ammeter to the receiving electrode. Graph of current verses the distance between electrodes is plotted in Fig. 4.

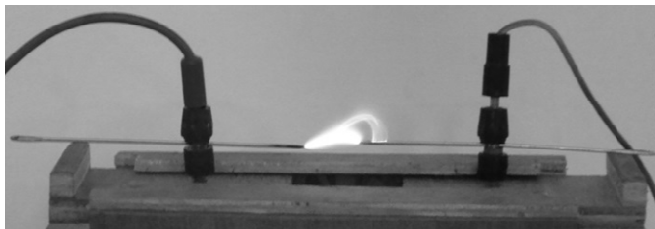


Fig. 3: Electric arc is seen upon providing electric supply to the High Voltage (HV) plate of TV.

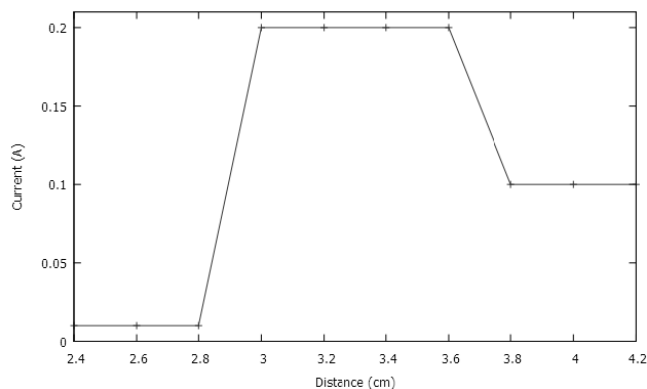


Fig. 4: Variation of the current received by the electrode with change in distance between the electrodes.

From the Fig. 4, irregular variation of the current with distance between the electrodes is evident. In the beginning, when the distance between the electrode is large i.e. around 3.8 to 4.2 cm, breakdown current of 0.1 A was recorded which can be attributed to initiation of sparking between the electrodes. It becomes still larger at 0.2 A for distances 3 to 3.6 cm suggesting more ionization of air due to reduction in distance between the electrodes. Further reduction in the distance between electrodes decreases the current by an order of magnitude. At 2.8 cm and below distance, current is only 0.01 A. Reason for this is generation of electric arc at these distances. Heat produced from the power losses (I^2R , I: Current, R: Resistance) maintains the ionization of air [5, 6]. Hence overall current received by the electrode reduces to significant extent during arc formation. Nonlinear relationship of current with voltage is also evident from the Fig. 4.

Apart from the electrical characterization, students may engage in optical characterization of the electric arc with the help of fiber optic spectrometer (ocean optics HR2000). They may point probe of spectrometer towards the electric arc to record the

spectrum. Fig. 5 shows the results from such measurement. Due to breakdown of air, continuum of radiation from 200 nm to 1100 nm got created. Several prominent peaks of Nitrogen are seen in Fig. 5. Apart from it absorption deep at 943 nm is visible. This absorption deep is due to atmospheric water vapor content/humidity. Humidity of air was 75% during the experiment.

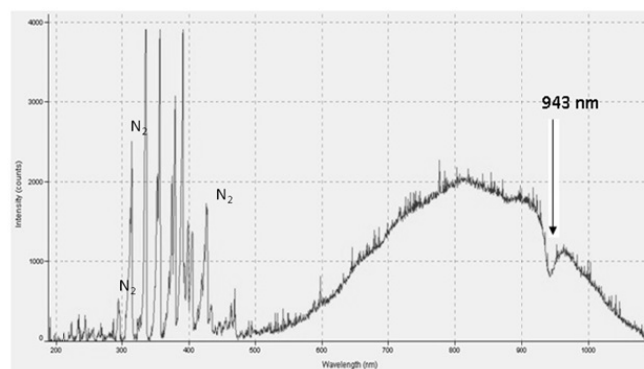


Fig. 5: Continuum of radiation as recorded by the fiber optic spectrometer.

3. Conclusion

Classroom/laboratory demonstration of dielectric breakdown of air using electronic waste generated lots of interest not only among students but other fellow teachers also. Air breakdown physics is complex and highly nonlinear but it is very interesting to watch it and do some basic measurement with some proper precautions. This particular set up is remote controlled. Hence one can operate it by maintaining some safe distance. Lots of other aspects of Air breakdown Physics is left unexplored here for the readers/teacher/instructors to explore [6].

Acknowledgements

I am thankful to my students Mr. Abdul Shafique, Mr. Mohammad Aqueel and Mr. Vinod Shinde for participating in this project.

References :

- [1]. Philip Krider, Physics Today 59, 42 (2006).
- [2]. Russell Alexander, Proc. Phys. Soc. London 20, 49 (1906).

-
- [3]. Paul A. Tipler, College Physics (Worth Publishers, 1987)
- [4]. Sankar P B, M.Tech Thesis, NIT Rourkela (2011).
- [5]. Vikramjit Singh , M.Sc(Tech) Thesis, Aalto University (2012).
- [6]. A Shafique, V Shinde, M Aqueel and K Alti, Journal of Pure and applied research in Engineering and Technology 2, 312 (2014).
-

Laser Zap: An Optical Approach for Elemental Analysis of Sample surfaces

²Zeenab A. Pathan, ¹Raja V.L.N. Sridhar, ²S.B.Patil, ¹Adwaita Goswami, ¹Kalpana Aravind and
¹Laxmiprasad A.S.

¹Laboratory for Electro-Optics Systems (LEOS),
Indian Space Research Organization, Bengaluru, 560058, India
²Department of Ceramics and Cement Technology,
PDACEK, Kalaburgi, 585102, India

Submitted On 31-03-2017

Abstract

LASER, the noble invention of 19th century has turned as a key solution in several scientific and engineering domains. Its prominence is well known by diverse applications ranging from the ground use to the space use. One of such potential applications of the laser is in use of sample characterization i.e., the elemental composition study of a target sample. Past two decades have shown its simplicity, ability and versatility in performing elemental analyses of samples on ground for pollutant analysis, impurity estimations, hazardous material detection etc., from close by and for remote distances. This technique is known as 'Laser Induced Breakdown Spectroscopy (LIBS)', in which a high-intense laser zaps the sample surface. Recent decade has witnessed a rejuvenated interest in application of the LIBS for planetary surface exploration missions to carryout in-situ and/or stand-off chemical analysis. The space agencies; NASA, ISRO, JAXA and ESA are channelizing their efforts in realization of an instrument based on LIBS to study planetary surfaces. This article primarily sheds light on concepts of LIBS technique along with details in brief on the realized experimental bench-top test setup and carried out in-situ investigations on terrestrial soil samples in ambient air based on the micro-LIBS approach.

1. Introduction

The theory of stimulated emission of radiation proposed by Einstein early in 1917 [1], made the laser existence possible. Since then, the lasers have contributed to humanity as a powerful scientific tool for expanding human knowledge and in its many applications that help people directly. In the last 5 decades, they have become ubiquitous, finding utility in thousands of highly varied applications in every section of modern society, including consumer electronics, information technology, science, medicine, industry, law enforcement and the military. It has assumed many forms ranging in size from tiny semiconductor devices no bigger than a grain of salt to high-power instruments as large as an average living room. The benefits of lasers in various applications stems from their properties such as coherency, high monochromaticity and capability for reaching extremely high powers. This article is associated with the last property of laser beam that can be employed to evaporate sample surfaces for simultaneous multi-element analysis of matter in any of its diverse forms, namely, solid, liquid or gas. Analytical techniques based on emission of electromagnetic radiation produced after excitation of atoms, ions or molecules present in a sample have been around for quite a while. Usually, these techniques employ some type of energy source to promote the species present in the sample to higher energy levels from where they decay, emitting characteristic radiation that is collected, sent to a

wavelength selector and detected. However, some of the analytical techniques, namely, atomic absorption spectroscopy, mass spectroscopy, EDAX (Energy-Dispersive X-ray Spectroscopy), XFS (X-ray Fluorescence Spectroscopy), APXS (Alpha Proton X-ray induced Spectroscopy); cannot deal directly with the original samples and sometimes some type of sample treatment must be performed prior analysis. Although the measurement step is rapid, precise and sensitive, sample treatment is often slow, cumbersome and prone to induce errors due to contamination and losses. Furthermore, the necessity of sample treatment limits the use of these techniques in the field. A requirement has been increasingly under investigation to match the interests of process analytical chemistry, environmental chemistry, forensic analysis, archaeological analysis, impurity analysis in ornaments and many others areas of science that present effectual arguments to realize an instrument that offer noncontact of sample under investigation. This paper describes a modern analytical technique based on atomic emission spectroscopy that employs a short pulse of high peak power radiation generated by a laser focused on a sample, in order to attain representative vaporization and excitation to create the 'plasma', which during its cool down emanates signatures of the elements present in sample in form of line emissions. This method is popularly known as 'LIBS' (Laser Induced Breakdown Spectroscopy), however in few of literature work and review books it is named as LIPS (Laser Induced Plasma Spectroscopy), LAAS (Laser Ablation Assisted Spectroscopy) [2,3].

2. Laser Induced Breakdown Spectroscopy (LIBS)

LIBS, is one of the atomic emission spectroscopy (AES) techniques that uses a short duration laser pulse as an excitation source. Figure-1 shows artistic representation of the basic phenomenon involved in LIBS technique. As shown in the figure, high-powered laser pulse is focused on a sample to create a plasma or laser spark. This spark imparts enormous power density (typically in order of few GW/cm^2) on interacting with the target surface that

heat up the surface, which in turn cause ablation, vaporization, atomization and ionization of the target. Thus the formation of micro-plasma in the focal volume of the laser pulse that excites the ablated atoms does occur. Thus, in the first instants, the atomic and molecular structure of the sample will be broken and heated, causing vaporization of a small fraction of the material (from hundreds of ng to a few μg). This vaporized material may contain free neutral atoms, ions, molecular fragments and free electrons. Further the incoming energy of the same laser pulse can sustain high temperature plasma ($> 10,000 \text{ K}$) in which the vaporized species can be excited and return later to their less energetic levels by emitting electromagnetic radiation. The emitted radiation is analyzed and the intensities are recorded by feeding the radiation in to a high-resolution spectrograph that registers the spectra. The LIBS spectrum contains large, redundant and complex information describing the elemental composition of the target. Each element has its unique emission lines working as the "fingerprint" of the element. After being spectrally resolved, the wavelength of the emission lines is used to identify the existence of the elements (qualitative analysis) and the background-subtracted peak intensity at the chosen emission line wavelength is used to quantify the elemental composition of the target (quantitative analysis).

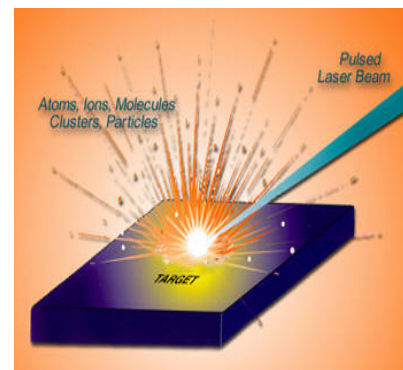


FIG. 1: Artistic representation of laser ablation phenomenon
(Courtesy: <https://blogs.maryville.edu>)

Recent years has shown a rejuvenated interest to use laser-induced breakdown spectroscopy (LIBS) as a field-deployable tool for elemental analysis. The analytical interest of the LIBS technique has resulted because of the multi-element capability, almost non-destructive approach, fast response and capability of

in situ analysis This technique has dominated the analytical atomic spectroscopy scene much like mainly because of the significant improvements that have been achieved in both laser and detector technology. The last 36 years have witnessed the results of the efforts made by a number of companies and research laboratories towards the development of commercial instruments, of new applications and of theoretical models providing a profound insight into the fundamentals of LIBS and associated phenomena. In addition to the application of LIBS for ground applications, the last half decade has imprinted the adaptation and realization of LIBS based instruments for space applications aiming at surface geochemistry by means of landers and/or rovers on the Mars and the Moon [4, 5]. In particular, through repeated irradiation over the same spot, depth profiling of the samples is also possible. This aspect is significant in planetary surface analysis in order to investigate the layer structured composition, if exist on planetary surface as well as aid in removing dust layers on target samples prior acquisition of true plasma emission spectrum.

3. Typical instrumentation aspects

The essential requirements for making LIBS measurements are a laser source (as an excitation medium), an optical system (to focus and transmit the high peak power laser radiation to the sample and to collect the plasma light emanating from the sample surface; diverting it to the spectrograph) and a spectrometer (to capture the plasma emission). Figure-2 shows the block diagram of LIBS test setup realized during experimental investigations at author's end.

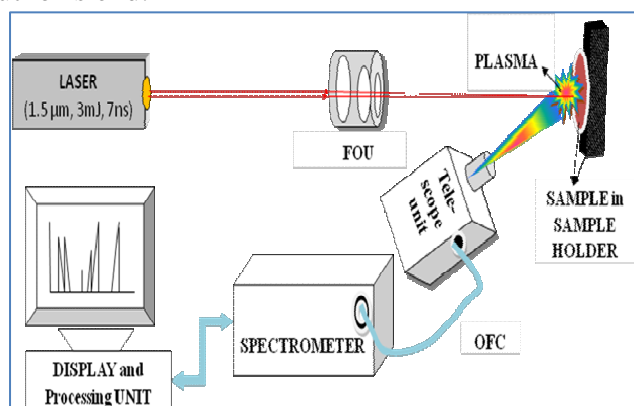


FIG. 2: Cartoon diagram of a typical LIBS setup

Though, there are varieties of sources that can generate plasma, laser has been considered as a source because of its ability to generate the majority of its output energy within a very narrow spectral range. Analytically useful laser plasmas can be generated with infrared, visible and ultra-violet wavelengths. Properties of lasers important for LIBS include wavelength, pulse energy and focused pulse power density. A key requirement of the laser and associated optical transmission system is that the power density at the sample surface shall be sufficient enough to produce both ablation of the sample and the formation of luminous plasma. Typical power density used for LIBS approach range from 0.4 GW/cm^2 to 4 GW/cm^2 . Such high power densities can easily be achieved using a pulsed and q-switched laser having moderate pulse energies. Pulse width typically used for LIBS is found to be in the range of 5-20 ns. With such pulse durations, a mill-joule laser in range of 3 mJ – 10 mJ coupled with a focusing optic system than can generate a spot size in range of $50 \mu\text{m}$ to $100 \mu\text{m}$ (diameter) is sufficient enough to produce the required powered density on the target sample surface to perform close by distance analysis (~ from 200 mm to 300 mm). Traditional LIBS systems use either a lens-based or a mirror-based system to collect the plasma light from the target surface. The collected light is either can be directly send to the entrance slit of spectrometer or transmitted via fiber optic cable. The spectrometer is basically a dispersion system that splits the collected light in to discrete wavelengths. Typical spectral range for LIBS application can be from 200 nm to 800 nm. The dispersed light is then guided to an opto-electronic detector (basically a linear/area CCD or a photo detector array) and processing system that reads the signal and displays the output in form of a spectrum (signal versus wavelength).

4. Realized bench-top experimental test-setup and investigations

This section of the article sheds light on the carried out experimental investigations in author's laboratory, based on micro-LIBS approach (means,

spot radius at the target surface is in range of 25 μm – 40 μm) for in-situ (from a distance of 200 mm from the target surface) elemental analysis of terrestrial soil samples. A low energy pulsed laser operating at 1.54 micron is used as excitation source. The peak power of laser pulse is 0.4 MW/cm^2 . As shown in Figure-2, the laser beam is passed through a 3-lens based focusing optics unit which is able to generate a spot size of 60 micron diameter on the sample kept at a distance of 200 mm. The plasma light is collected by means of a telescope unit (comprise a pair of lenses) and then diverted to the spectrograph system via a fiber optic cable of length 1 meter. The spectrometer consists of 7-channel dispersion modules covering the wavelength range from 200 nm to 980 nm providing a spectral resolution of 0.1 nm. Operation control data acquisition and data interpretation software modules of spectrometer are installed in to a computer system, which is mated to the spectrometer by means of interface modules. For experimental investigations nearly 60 types of standard and certified geochemical reference samples were procured in powder form in order to assess the in-situ ability of low-energy LIBS for qualitative and quantitative analysis. For a better approach of investigations, prior experiments all procured samples are segmented and classified as per their category, namely, rocks and stones, fine powder, clay, slag, soil, sand, sediments, ore and minerals etc. As shown in Figure-3, all these samples of pelletized into a circular disc of 13 mm diameter and 7 mm thickness for investigations. The inset figure at the bottom right corner shows the snap shot of procured samples. Experiments are carried out both on power as well as pellet stats of the sample to find out similarities and vice-versa.



FIG.3: Powder and Pellets of geological sample GBW07112

5. Results and discussions

Figure-4 presents acquired plasma emission spectra of 3 geological samples, i.e., JP-1, Dolomite, and SX09-11, which vary in composition of elemental oxides, namely, SiO_2 , CaO , MgO , Al_2O_3 , Fe_2O_3 , TiO_2 , Na_2O , K_2O , Cr_2O_3 etc. 3-different intensity scales can be seen in the figure, due to the compositional variation of elements in samples. Each peak of the emission spectrum represents the presence of respective element. Obtained line emission wavelengths are compared with NIST atomic data base to find out the elements. Figure-5 shows the processed and qualitative analyzed plasma spectrum of sample JP-1.

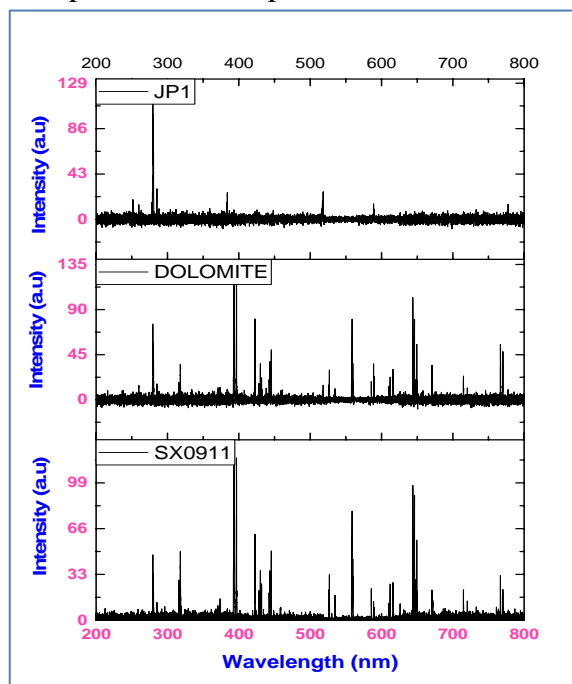


FIG.4: Plasma spectra of samples JP-1, Dolomite and SX09-11

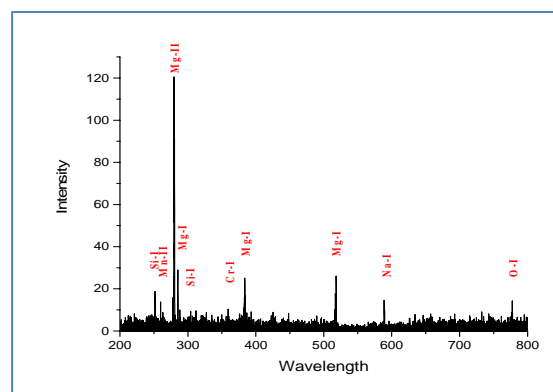


FIG.5: Qualitatively analysed plasma spectrum of JP-1 sample

To assess the quantitative capability of micro-LIBS, a set of 6 samples data sets varying in 'Mg' concentration were analyzed.

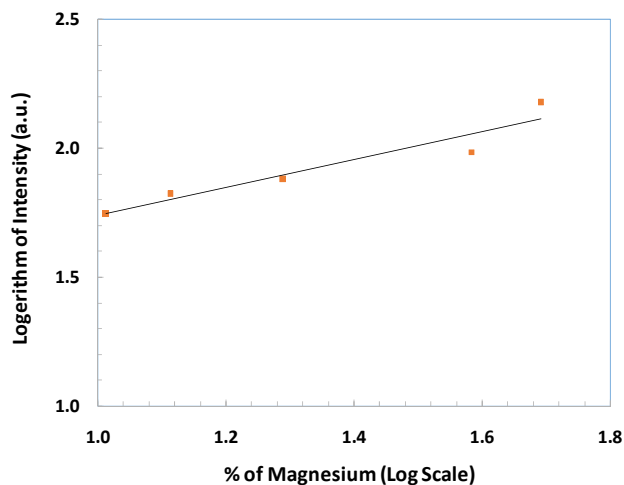


FIG. 6: Calibration curve for 'Mg' in Geological standard samples

Figure-6 shows calibration curve for magnesium element at emission wavelength of 279.5 nm. Log-Log linear regression method applied to find the best R^2 value. The correlation found was $R^2 = 0.96$, which is very satisfactory given the different compositions of samples. In order to test the robustness of the calibration curve, one reference materials was used: the JP-1. The reference value for 'Mg' concentration is 44.6%. The value measured by low-energy LIBS is 43.06%. Thus, a good agreement was obtained with the reference values within the measurement error.

6. Conclusions

Over the recent years, the laser induced breakdown spectroscopy (LIBS) technique has been applied in

several fields. The main advantage of LIBS is the capability to obtain rapid and relatively non expensive measurements with minimum sample preparation. Varieties of commercial LIBS based instruments are being developed to suit the application requirement. LIBS applicability for in-situ detection of elemental analysis is of current interest. Suitability and analytical capability of LIBS for in-situ elemental analysis (at a distance of 200 mm from sample surface) is explained in this work employing a compact laser source of 3-mJ energy. A good agreement was obtained with the standard values within the measurement error.

7. Acknowledgements

Authors would like to express their sincere gratitude to the PPED and Director of LEOS-ISRO for providing the platform to take up such challenging and promising tasks.

8. References

- [1] Einstein, A.; *Phys. Z.*, 18, 121, (1917).
- [2] L.J. Radziemski, *Spectrochim. Acta Part B*, 57, 1109–1113, (2002).
- [3]. P.K. Diwakar, D.W. Hahn, *Spectrochim. Acta Part B*, 63, 1038–1046, (2008).
- [4] R. C. Wiens et. al, *Space Sci Rev*, DOI 10.1007/s11214-012-9902-4, (2012).
- [5] A.S. Laxmiprasad et. al., *Journal of advances In Space Research*, <http://dx.doi.org/10.1016/j.asr.2013.03.021>, (2013).

Exploration of the Quantum Casimir Effect

A. Torode¹

¹Department of Physics And Astronomy, 4th year undergraduate (senior)

Michigan State University

East Lansing MI, 48823

torodean@msu.edu

Submitted on 04-05-2017

Abstract

Named after the Dutch Physicist Hendrik Casimir, The Casimir effect is a physical force that arises from fluctuations in electromagnetic field and explained by quantum field theory. The typical example of this is an apparent attraction created between two very closely placed parallel plates within a vacuum. Due to the nature of the vacuum's quantized field having to do with virtual particles, a force becomes present in the system. This effect creates ideas and explanations for subjects such as zero-point energy and relativistic Van der Waals forces. In this paper I will explore the Casimir effect and some of the astonishing mathematical results that originally come about from quantum field theory that explain it along side an approach that does not reference the zero-point energy from quantum field theory.

1 Introduction And History

The Casimir effect is a small attractive force caused by quantum fluctuations of the electromagnetic field in vacuum (Figure 1). In 1948 the Dutch physicist Hendrick Casimir published a paper predicting this effect [1, 2]. According to Quantum field theory, a vacuum contains particles (photons), the numbers of which are in a continuous state of fluctuation and can be thought of as popping in and out of existence [3]. These particles can cause a force of attraction. Most generally, the quantum Casimir effect is thought about in regards to two closely parallel plates. As the plates are brought together, Casimir realized that between them, only those virtual photons whose wavelengths fit a whole number of times should be counted whilst calculating the vacuum energy [1]. This leads to a decrease in energy density between the plates as they are moved closer which implies that a small force is drawing them together. similarly

you can say that due to the smaller space between the plates only smaller exotic particles can exist between them. From this difference in particles outside the plates and those between the plates, a small pressure change can be calculated which creates a force pushing the plates towards one another [3]. This force is the Casimir effect.

In 1996, the small force was measured to within 5% uncertainty to that of the theoretical prediction by Steven Lamoreaux [4]. All bosons make a contribution to the Casimir force, but fermions make a repulsive contribution to the force. All of these particles make a contribution to the force though only that from photons is measurable. The theory states that the lowest energy state of a vacuum (the zero-point energy) is infinite when considering all possible photon modes. The original Casimir force derivation comes about from a situation in which the differences in infinities cancel out which arises from very interesting mathematics. There are inconsistencies and puzzles that arise from the existence of this effect, especially when applying it to the theories of quantum gravity. The solutions to these inconsistencies are however expected to be found within the solution to a theory of quantum gravity [1].

In 2005, Jaffe made it clear that the zero-point fluctuations formulated in quantum field theory was not observable in any laboratory experiments though the vacuum value of the stress tensor (energy density of the vacuum) $\langle T_{\mu\nu} \rangle \equiv -\epsilon g_{\mu\nu}$ even appears in

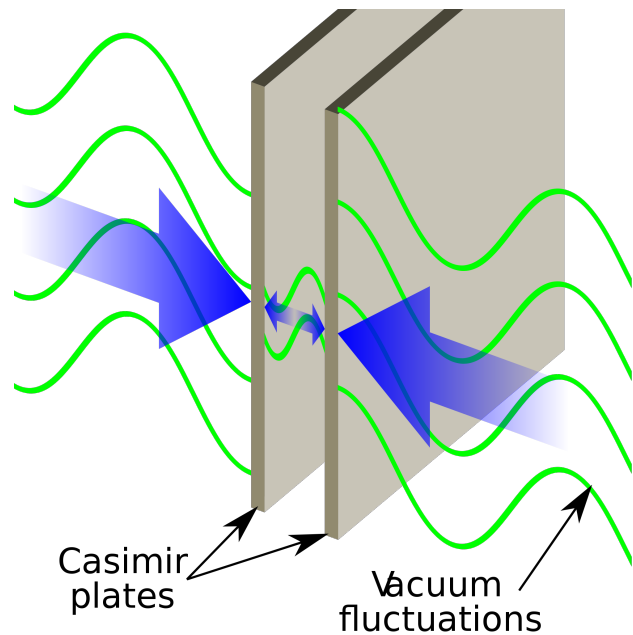


Figure 1: A simple diagram of two parallel plates and a representation of vacuum fluctuations [5].

the right hand side of Einstein's equation for gravity in general theory of relativity [6]

$$\frac{1}{2}g_{\mu\nu}R - R_{\mu\nu} = 8\pi G(\tilde{T}_{\mu\nu} - \epsilon g_{\mu\nu}). \quad (1)$$

Jaffe also demonstrates in his paper that you can calculate the Casimir force without reference to the zero-point energy [6], which suggests that the zero-point energy may simply just be a nice mathematical construct in this situation to arrive at a measurable result. This will be discussed later in more detail.

2 'Astounding' Mathematical Results.

One of my favorite results I have encountered in my studies (which led me to the

Casimir effect) follows as

$$\sum_{n=1}^{\infty} n \rightarrow -\frac{1}{12}. \tag{2}$$

This result does not explicitly make sense because the sum in equation (2) is a divergent sum. However, due to a process known as analytic continuation, some divergent sums can have a finite value. In 1913, this appeared in the work of a very famous mathematician from India, Srinivasa Ramanujan and is an important result for String Theory and other branches of physics. The Riemann zeta function

$$\zeta(s) = \sum_{n=1}^{\infty} \frac{1}{n^s} = 1 + 2^{-s} + 3^{-s} + 4^{-s} + \dots \tag{3}$$

is widely studied and used often in physics. In quantum physics, the energy density of a vacuum should be proportional to $\zeta(-3) = 1 + 8 + 27 + 64 + \dots$, which is a divergent series and thus does not make much sense as an energy density [7]. When we write this using equation (3) and use the process of analytic continuation, this can be written

$$\zeta(-3) = \sum_{n=1}^{\infty} \frac{1}{n^{-3}} = 1 + 2^3 + \dots \rightarrow \frac{1}{120}. \tag{4}$$

The way Ramanujan expresses functions that are divergent such as this (from the Riemann zeta function) is

$$\sum_{k=\alpha}^x f(k) \sim \int_{\alpha}^x f(t)dt + c + \frac{1}{2}f(x) + \sum_{k=1}^{\infty} \frac{B_{2k}}{(2k)!} f^{(2k-1)}(x), \tag{5}$$

[8]. This is a process of analytically continuing these divergent series and coming up with a finite result without any 'magic'. I say magic because there is a process in which one can ignore (in a sense) the divergent nature of a sum and come up with these results as well.

As an example, I will give a 'proof' of equation (2) using this method, which was first shown by Euler around 1735 [9]. Consider the following well defined sum

$$f(x) = 1 + x + x^2 + x^3 + x^4 + \dots = \frac{1}{1-x}, \tag{6}$$

for $|x| < 1$. Differentiating this gives

$$f'(x) = 1 + 2x + 3x^2 + \dots = \frac{1}{(1-x)^2}. \tag{7}$$

If we evaluate the result at $x = -1$ we get

$$f'(-1) = 1 - 2 + 3 - 4 + \dots = \frac{1}{4}. \tag{8}$$

Note that this is troublesome because we defined $f'(x)$ based on a function only valid for when $|x| < 1$. However, for our purposes suppose we can extend our limits and make $f(x)$ differentiable at $x = -1$. Now, if we take $2^{-s}\zeta(s)$ we have

$$\begin{aligned} 2^{-s}\zeta(s) &= 2^{-s} \sum_{n=1}^{\infty} \frac{1}{n^s} = \sum_{n=1}^{\infty} \frac{2^{-s}}{n^s} \\ &= 2^{-s} + 4^{-s} + 6^{-s} + 8^{-s} \dots \end{aligned} \tag{9}$$

Now, if we take $g(s) = [1 - 2(2^{-s})]\zeta(s)$ we

have

$$\begin{aligned}
 g(s) &= [1 - 2(2^{-s})]\zeta(s) \\
 &= \zeta(s) - 2(2^{-s})\zeta(s) \\
 &= 1 + 2^{-s} + 3^{-s} + 4^{-s} + 5^{-s} + 6^{-s} + \dots \\
 &\quad - 2(2^{-s} + 4^{-s} + 6^{-s} + \dots) \\
 &= 1 - 2^{-s} + 3^{-s} - 4^{-s} + 5^{-s} - 6^{-s} + \dots
 \end{aligned} \tag{10}$$

Finally, if we set $s = -1$, we can see that $g(-1) = \zeta(-1) - 2(2)\zeta(-1) = -3\zeta(-1)$ and evaluating this from equation (10) and then using our result from equation (8) gives us

$$\begin{aligned}
 -3\zeta(-1) &= 1 - 2 + 3 - 4 + \dots = \frac{1}{4} \\
 \implies \zeta(-1) &= -\frac{1}{12}. \tag{11}
 \end{aligned}$$

Now, notice that plugging in $s = -1$ into the Riemann zeta function gives us the same result from equation (2) and thus

$$\zeta(-1) = -\frac{1}{12} \implies \sum_{n=1}^{\infty} n \rightarrow -\frac{1}{12}. \tag{12}$$

This result is very important to obtaining the $24 + 2 = 26$ dimensions in bosonic string theory [10]. It is also a simpler example than that of equation (4) to illustrate.

3 Casimir Force Derivation.

In Casimir’s original paper, he did not use the result in equation (4) explicitly, though in a more recent derivation assuming zeta-regularization, one can see how it is obtained. Let $k_x, k_y,$ and k_z represent the wave

numbers in the x, y and z directions respectively. If we allow two plates to be parallel in the $x - y$ plane at a distance a apart, then we can define the cavity between the plates by

$$0 \leq x \leq \sqrt{A} \tag{13}$$

$$0 \leq y \leq \sqrt{A} \tag{14}$$

$$0 \leq z \leq a, \tag{15}$$

where the plates are a square of area A . If we adopt a periodic boundary condition, then we can show

$$k_x = \frac{2\pi n_x}{\sqrt{A}} \implies dn_x = \frac{\sqrt{A}}{2\pi} dk_x \tag{16}$$

$$k_y = \frac{2\pi n_y}{\sqrt{A}} \implies dn_y = \frac{\sqrt{A}}{2\pi} dk_y \tag{17}$$

$$k_z = \frac{n_z \pi}{a}, \tag{18}$$

with $(n_x, n_y, n_z) \in \mathbb{Z}$. The frequency of this wave is $\omega_n = v|\vec{k}| = v\sqrt{k_x^2 + k_y^2 + k_z^2}$. If we assume we are in a vacuum, then the speed of any electromagnetic wave is just c and thus $\omega_{n_z} = c\sqrt{k_x^2 + k_y^2 + k_z^2}$. The vacuum energy is the sum over all possible modes. The zero-point (ground state) energy associated with the n_z^{th} mode is given by $E_{n_z} = \frac{\hbar\omega_{n_z}}{2}$. The energy of all combined modes is then the sum over all n_z or $E = \sum_{n_z=1}^{\infty} \frac{\hbar\omega_{n_z}}{2}$. For simplicity we can allow $n \equiv n_z$. Taking the expectation value of the energy over the entire area of the plates can be done by integrating over all possible values of n_x, n_y and

all possible expectation modes which yields

$$\langle E \rangle = \frac{\hbar}{2} \iint \sum_{n=1}^{\infty} \omega_n dn_x dn_y \quad (19)$$

$$= \frac{A\hbar}{8\pi^2} \iint \sum_{n=1}^{\infty} \omega_n dk_x dk_y. \quad (20)$$

This expression is clearly infinite due to the diverging sum. If we use zeta-regulation, we can find a finite energy per unit area by defining a quantity $\langle E(s) \rangle$ which goes to equation (20) when $s=0$.

$$\begin{aligned} \frac{\langle E(s) \rangle}{A} &= \frac{\hbar}{8\pi^2} \iint \sum_{n=1}^{\infty} \omega_n |\omega_n|^{-s} dk_x dk_y \quad (21) \\ &= \frac{\hbar}{8\pi^2} \sum_{n=1}^{\infty} \int \int \omega_n |\omega_n|^{-s} dk_x dk_y. \end{aligned} \quad (22)$$

Simplifying the above expression (Using Mathematica to take the integral over dk_x and dk_y) gives us

$$\frac{\langle E(s) \rangle}{A} = \frac{\hbar c^{1-s} \pi^{2-s}}{2a^{3-s} (3-s)} \sum_{n=1}^{\infty} |n|^{3-s}. \quad (23)$$

This may then be analytically continued to $s = 0$ where it becomes finite when using equation (4).

$$\frac{\langle E \rangle}{A} = \lim_{s \rightarrow 0} \frac{\langle E(s) \rangle}{A} = -\frac{\hbar c \pi^2}{6a^3} \zeta(-3). \quad (24)$$

Now, plugging in equation (4) in the above expression gives us

$$\frac{\langle E \rangle}{A} = \frac{-\hbar c \pi^2}{720a^3}. \quad (25)$$

The Casimir force per unit area between two parallel plates within a vacuum is therefore given by $F = -\nabla \langle E \rangle$ which is

$$\frac{F_c}{A} = -\frac{d \langle E \rangle}{da A} = \frac{-\hbar c \pi^2}{240a^4}. \quad (26)$$

As we can clearly see, this result would not have come about without the use of analytical continuation. In a sense, this is due to nature not containing apparent infinities. Rather, the continuation allowed us to arrive at a finite solution which is experimentally confirmed. The fact that our expression came out negative suggests that the force is an attractive force and due to the presence of \hbar , we can see that the force is of a quantum origin. In the original derivation, Casimir computed non-convergent sums using Euler-Maclaurin summation with a regularizing function [2].

4 Implications From The Zero-Point Derivation.

The Casimir effect extends quantum field theory to allow for negative energy densities with respect to the ordinary vacuum energy. It has been suggested by numerous physicists such as Stephen Hawking, Kip Thorne, and many more that such a thing will allow the possibilities of stabilizing traversable wormholes [11]. Miguel Alcubierre, creator of the Alcubierre Drive has also suggested using the Casimir effect to obtain negative energy required for his designs [11]. In many cases, this effect has been shown to have possible applications in propulsion drives for space craft. It also has possible application in nanotechnology which has been suggested by some [11]. Due to the small scale that this force is observed on, this would make sense that it

could present possible applications in nanotechnology. For instance, the force of attraction could be used as an architecture for moving components on a microscopic scale or something much more complex.

5 Casimir Force Without Referencing Zero-Point Energy.

As mentioned earlier, Jaffe argues that the Casimir force can be constructed without considering zero-point fluctuations of quantized electromagnetic field and is a result from the material of the plates and not resulting from zero-point energies. If we use the Drude model of metals, then the metal/conductor properties are characterized by a plasma frequency ω_p and a skin depth δ . The original result does not depend on anything other than the distance of the plates and fundamental constants. However, this result assumed that the plates were perfect conductors which do not exist in reality. The skin depth of a material is a measure of how far electromagnetic waves penetrate through a material and thus can cause a relationship between the waves within the plates to those outside.

Jaffe argues that both ω_p and δ are dependent on the fine structure constant α . He then argues that the perfect conductor approximation is good for sufficiently large α which in the case of the Casimir measurement scales for experimental verification are satisfied by the physical value of $\alpha \approx 1/137$ which is why the original derivation is sup-

ported by experimental results. Similarly, he also argues that the Casimir force vanishes as $\alpha \rightarrow 0$.

6 Conclusion

I have shown that while referencing zero-point energy one can derive the Casimir force using zeta-function regularization, however, it can also be calculated without reference to the zero-point energy which suggests that it may not be related to the energies that are suggested to come about from quantum field theory but instead the fine structure constant and properties of materials. It is fascinating to note that the same experimentally observed result can be obtained through a simple method using zeta-function regularization and ignoring divergences which may possibly suggest that this is a useful mathematical construct that could potentially have many real world applications. Much like the early use of imaginary numbers, which appeared to have no physical application, it may prove to be a useful method of mathematical manipulation that could lead us to new unique breakthroughs much like in the case of the Casimir force.

Acknowledgments

This work was originally compiled as a poster presentation for a class project. I gratefully acknowledge the help of S.D Mahanti for suggesting I convert the project into this paper and proofreading/correcting

my work. I would also like to acknowledge the help of C. Piermarocchi for assistance with the original project.

References

- [1] Gibbs, Philip. "What Is the Casimir Effect?" The Casimir Effect. University of California, 1997. Web. 16 Oct. 2016.
- [2] H.B.G. Casimir, Proc. Kon. Ned. Akad. Wetensch. B51, 793 (1948)
- [3] Casimir Effect & Black Holes - Sixty Symbols. Prod. Brady Haran. Perf. Mike Merrifield Ph.D. Youtube. University of Nottingham, 20 Mar. 2014. Web.
- [4] S. Lamoreaux, Phys. Rev. Lett. 78, 5 (1996)
- [5] Image from https://en.wikipedia.org/wiki/Casimir_effect
- [6] Jaffe. R. L. "Casimir effect and the quantum vacuum" 10.1103/PhysRevD.72.021301. 2005.
- [7] Berman, David. "Infinity or $-1/12$?" Plus.maths.org. +Plus Magazine, 18 Feb. 2014. Web. 16 Oct. 2016.
- [8] Library of Congress Cataloging in Publication Data Ramanujan Aiyangar, Srinivasa, 1887-1 920. Ramanujans notebooks. Mathematics- Collected works. 1. Berndt, Bruce C., 1939- II. Title. QA3. R33. 1985. 510. 84-20201
- [9] John Baez on the number 24. The Rankin Lectures 2008. Youtube. John Baez. University of California. 16 May. 2012. Web.
- [10] Sum of Natural Numbers (second proof and extra footage). Prod. Brady Haran. Perf. Ed Copeland Ph.D and Tony Padilla Ph.D. Youtube. University of Nottingham, 11 Jan. 2015. Wb.
- [11] Casimir effect. (n.d.). Retrieved October 16, 2016, from https://en.wikipedia.org/wiki/Casimir_effect#cite_note-45

Rheology in the Teaching Lab: Properties of Starch Suspensions

J. A. Groman¹, J. I. Katz² and J. G. Miller³

¹Department of Physics
Washington University, St. Louis, Mo. 63130, U. S. A.
jgroman53@yahoo.com

²Department of Physics and McDonnell Center for the Space Sciences
Washington University, St. Louis, Mo. 63130, U. S. A.
katz@wuphys.wustl.edu

³Department of Physics
Washington University, St. Louis, Mo. 63130, U. S. A.
james.g.miller@wustl.edu

Submitted on 07-June-2017

Abstract

In everyday life we encounter many complex fluids, from shear-thinning paint and toothpaste to shear-thickening starch suspensions. The study of their properties offers an opportunity for students to relate sophisticated physical concepts to their everyday experience. Modern rheology uses expensive equipment impractical for the teaching laboratory. Here we describe a rudimentary rheometer suitable for student laboratories that can demonstrate and quantify discontinuous shear thickening, the most dramatic property of complex fluids, and use it to measure the properties of starch suspensions.

The rheometer results agree with theory for a viscous Newtonian fluid, but the behavior of shear-thickening starch suspensions is unexpectedly complex.

1 Introduction

Simple fluids, such as water, honey, oils, pitch and liquid nitrogen have the property that their stress is proportional to their strain rate (flow rate). Their ratio is a scalar viscosity. This proportionality defines a simple (or “Newtonian”, because Newton was the first to formulate this relation) fluid, what-

ever the value of the viscosity, and describes equally well fluids of low viscosity (water, liquid nitrogen), larger viscosity (oils, honey) and even fluids whose viscosity is so high that noticeable flow may require many years (pitch).

In contrast, there are “non-Newtonian” fluids with more complicated relations between stress and strain rate. These fluids may contain polymers, or be suspensions (typically in a Newtonian solvent) of solid particles, membrane-bound vesicles or droplets of an immiscible fluid (emulsions). The study of such fluids is called rheology, and many complications are possible. Some have a viscosity that decreases as the rate of flow increases; these are called “shear-thinning”, and some of these (“Herschel-Bulkley” fluids) have a small strength that must be overcome in order that they flow at all. Others have a viscosity that increases, either gradually or discontinuously, as the rate of flow increases; these are called “shear-thickening”. Yet others, such as starch suspensions, display combinations of these behaviors.

Paint, ketchup, toothpaste and corn starch suspensions are familiar examples of non-Newtonian fluids [1]. Most of these are shear-thinning: they may have a small finite strength at rest (which is why toothpaste doesn't flow out of its tube unless squeezed, or ketchup out of its bottle, unless squeezed, shaken or struck) or a viscosity that decreases as the flow rate is increased (so that paint is easily spread with a

brush, but doesn't drip once spread). Unlike these, starch suspensions have the remarkable property, known to schoolchildren who gave them the nickname “oobleck” after a fictional substance, of suddenly turning stiff, increasing their viscosity by orders of magnitude, if the strain rate exceeds a threshold. This phenomenon is known as discontinuous (abrupt) shear thickening (Brown and Jaeger [2]).

Measurement of the viscosity of Newtonian fluids is a familiar experiment in advanced undergraduate laboratories, but experiments involving non-Newtonian fluids have been few [3, 4, 5, 6, 7, 8], and none of them have addressed the striking phenomenon of discontinuous shear thickening. A student laboratory experiment will excite more interest if it is novel, if it explores a dramatic phenomenon, if it is related to students' everyday experience and if it reveals a phenomenon at the research frontier that is incompletely understood. The discontinuous shear thickening of starch suspensions meets these criteria. Yet quantitative rheometry requires expensive and delicate equipment unavailable in and unsuitable for the student laboratory. Here we describe, and report results obtained with, a rudimentary rheometer that can be assembled from a few dollars' worth of equipment. With the aid of a consumer-grade video camera, it produces quantitative data.

2 Methods

2.1 Apparatus

The apparatus is shown in Fig. 1. A light-emitting diode mounted on the top of the rod was used to determine the position of the rod against an aligned meter stick with an attached LED that serves as a reference. Data were recorded with a video camera at one or 30 frames per second (the lower recording rate was used for more slowly sinking rods because of limited memory), and the velocity averaged over 20 frames if recorded at 30 fps and over 5 frames if recorded at 1 fps. Averaging was necessary because the rod position was determined to only ± 0.5 line in the video image, or about ± 0.1 mm; accuracy was limited by the resolution of the video image. Data were processed with ImageJ software [9]. The rods were 36 cm long, rounded to a hemisphere at their lower ends, with diameters 18.9 mm. The guide sleeve had an internal diameter of 19.8 mm and was 12.5 cm long. The cylinder (a nominal 50 ml graduated cylinder but with additional volume above the graduations) had an internal diameter of 23.5 mm and depth, rim to interior bottom, of 16.5 cm. The aluminum rod had a mass of 271 g and the stainless steel rod a mass of 820 g. The essential parts of the apparatus are shown schematically in Fig. 2.

2.2 Theory

The flow of fluid around a solid rod sinking in a tube that is only slightly wider than



Figure 1: The rudimentary rheometer consists of a glass cylinder filled (empty in the photograph) with the fluid whose properties are to be measured. A metal rod, visible through the glass, with diameter slightly less than that of the cylinder sinks into the fluid, driving fluid up the annulus between rod and cylinder. The rod is guided and centered in the cylinder by a cylindrical sleeve (of copper, visible in the photograph alongside the meter stick) aligned with the cylinder axis. Also visible is the LED, taped to the upper part of the rod, whose light is used to measure the sink rate of the rod.

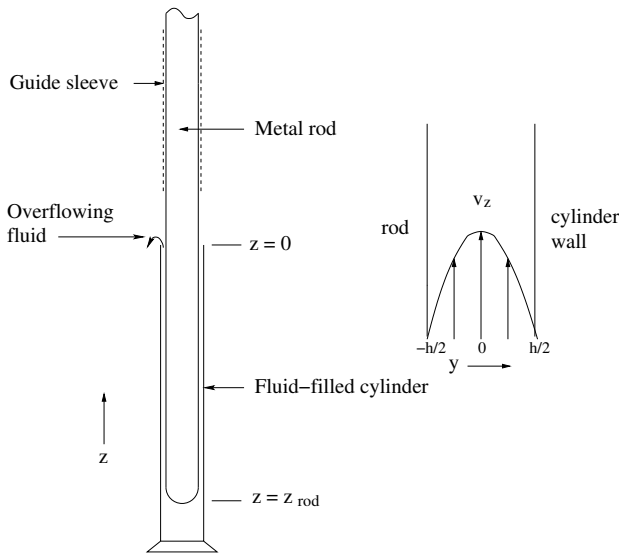


Figure 2: The essential parts of the rheometer (left) and the flow field in the thin annulus between the rod and the cylinder wall (right).

the rod itself may be divided into distinct regions. Underneath the rod is a pool of fluid whose width is the tube’s diameter and (until the rod almost reaches the bottom of the tube) in which the velocity is small because the cross-sectional area is large. The shear stress, proportional to the velocity divided by the diameter, is also small, and the pressure is, to good accuracy, uniform (aside from the variation of the hydrostatic head with depth) throughout this pool.

A second region consists of the narrow annulus between the rod and the tube. Its narrowness implies that the sinking of the rod must be accompanied by a much higher mean fluid velocity as the displaced fluid moves upward. In this narrow annulus the fluid velocity implies a large shear rate (derivative of velocity with respect to the ra-

dial coordinate) because the fluid velocity on the solid surfaces must equal the velocities of those surfaces, zero on the tube and equal to the rod’s sink rate on the rod. The shear flow implies a shear stress because the fluid is viscous.

If the width h of the gap between the rod and the tube is much less than the inner radius r of the tube ($h \ll r$) then this gap may be approximated as a planar duct. An elementary solution for flow in a planar duct, including the sinking rate of the rod, may be found.

The error introduced by these approximations is $O(h/r) \sim 10\%$ in our experiments. This is acceptable because our purpose is to demonstrate *qualitative* properties of non-Newtonian shear-thickened fluids (with a Newtonian flow to demonstrate the validity of the method). The full theory [10] of the flow in a cylindrical annular duct is cumbersome, too mathematically complex for student understanding, and not justified in experiments in which the geometry cannot be controlled precisely.

2.2.1 Newtonian Fluids

The flow of an incompressible Newtonian viscous fluid is described by the Navier-Stokes equation [11]

$$\frac{\partial \vec{v}}{\partial t} + (\vec{v} \cdot \vec{\nabla}) \vec{v} = -\frac{1}{\rho_f} \vec{\nabla} p + \vec{g} + \frac{\eta}{\rho_f} \nabla^2 \vec{v}, \quad (1)$$

where ρ_f is the fluid density, η is its dynamic viscosity, p is the pressure, there is a gravitational acceleration \vec{g} and \vec{v} is the

fluid velocity. Because the Reynolds number is $\ll 1$ in our experiments, any transients are rapidly damped and we consider steady flow ($\partial \vec{v} / \partial t = 0$).

Let z be the vertical coordinate, so that $\vec{g} = -g\hat{z}$, and y be the radial coordinate (Cartesian, in the planar duct approximation) in the duct formed by the surface of the rod and the inner wall of the tube. For convenience we take $y = 0$ midway between the surface of the rod and the inner wall of the tube, so that $-h/2 \leq y \leq h/2$. The fluid velocity $\vec{v} = v(y)\hat{z}$ is vertical and \vec{v} depends only on y , so that $(\vec{v} \cdot \vec{\nabla})\vec{v} = 0$. Taking $z = 0$ at the surface of the fluid (the open end of the tube, where displaced fluid overflows; Fig. 2) and $z = z_{rod} < 0$ at the bottom of the rod (of length L and density ρ_{rod} , immersed to a depth $|z_{rod}|$), the pressure $p(0) = p_{atm}$ and $p(z_{rod}) = p_{atm} + \rho_{rod}gL$. In our experiments $\rho_{rod} = 2.7 \text{ g/cm}^3$ for the aluminum rod and $\rho_{rod} = 8.0 \text{ g/cm}^3$ for the stainless steel rod.

The Navier-Stokes equation becomes

$$\eta \frac{d^2 v(y)}{dy^2} = \frac{\rho_{rod}gL}{z_{rod}} + \rho_f g \equiv \frac{dp'}{dz}, \quad (2)$$

where the effective pressure gradient dp'/dz includes the effect of buoyancy. The solution takes the form

$$v(y) = Ay^2 + By + C. \quad (3)$$

Using the boundary conditions $v(-h/2) =$

v_{rod} and $v(h/2) = 0$ we find

$$A = \frac{1}{2\eta} \left(\frac{\rho_{rod}gL}{z_{rod}} + \rho_f g \right) \quad (4)$$

$$B = -\frac{v_{rod}}{h} \quad (5)$$

$$C = -\frac{h^2}{8\eta} \left(\frac{\rho_{rod}gL}{z_{rod}} + \rho_f g \right) + \frac{v_{rod}}{2}. \quad (6)$$

The volume flow rate per unit length of rod circumference

$$\begin{aligned} \dot{q} &= \int_{-h/2}^{h/2} v(y) dy \\ &= -\frac{h^3}{12\eta} \left(\frac{\rho_{rod}gL}{z_{rod}} + \rho_f g \right) + \frac{v_{rod}h}{2} \end{aligned} \quad (7)$$

and the total volume flow

$$\begin{aligned} \dot{Q} &= 2\pi r \dot{q} \\ &= -\frac{\pi r h^3}{6\eta} \left(\frac{\rho_{rod}gL}{z_{rod}} + \rho_f g \right) + \pi r v_{rod} h. \end{aligned} \quad (8)$$

Equating \dot{Q} to the rate $-\pi r^2 v_{rod}$ at which the sinking rod displaces fluid leads to an equation for the sink rate of the rod:

$$v_{rod} = \frac{dz_{rod}}{dt} = \frac{h^3}{6\eta(r+h)} \left(\frac{\rho_{rod}gL}{z_{rod}} + \rho_f g \right). \quad (9)$$

From this we find that in Eqs. 7 and 8 the term involving v_{rod} is smaller than the preceding term by the factor $h/(r+h) \ll 1$. The stress $\eta dv(y)/dy$ on the surface of the rod exerts an upward force that may be evaluated using Eqs. 3–6 and 9. This viscous force is smaller than the upward force of the pressure in the pool below the rod by a factor $\approx h/r \ll 1$.

In order to simplify the integration we neglect buoyancy, the last term in Eq. 9;

buoyancy is never more than a 10% correction to the preceding term, and approaches 0% when $|z_{rod}| \rightarrow 0$ (the rod has just entered the fluid). Integration yields

$$z_{rod} = -\sqrt{\frac{h^3 g \rho_{rod} L}{3\eta(r+h)}} t^{1/2} \quad (10)$$

$$v_{rod} = -\sqrt{\frac{h^3 g \rho_{rod} L}{12\eta(r+h)}} t^{-1/2}, \quad (11)$$

where t is measured from the time the rod enters the fluid.

We use a guide tube to keep the sinking rod close to and parallel to the axis of the fluid-filled cylinder, but the positioning and

alignment cannot be perfect. Here we consider the effects of an off-center rod. Because the gap is everywhere narrow compared to the rod's and tube's radii ($h \ll r$), the theory may also be applied to off-center rods by integrating \dot{q} around the rod. If the axis of the rod is displaced from the axis of the cylinder by Δx ($\Delta x \leq h$) the width of the gap between rod and cylinder, to lowest order in the small quantity $\Delta x/r$, is

$$\Delta r(\theta) \approx h - \Delta x \cos \theta, \quad (12)$$

where θ is the angle from the direction of $\vec{\Delta x}$. Then

$$\dot{Q} = \int_0^{2\pi} d\theta r \dot{q}(\theta) = -\frac{\pi r h^3}{6\eta} \left(\frac{\rho_{rod} g L}{z_{rod}} + \rho_f g \right) \left[1 + \frac{3}{2} \left(\frac{\Delta x}{h} \right)^2 - \frac{h}{r+h} \right]. \quad (13)$$

The last term in the brackets is $\ll 1$ and can be neglected. Then for an off-center rod \dot{Q} and $v_{rod} = \dot{Q}/\pi r^2$ can be as much as 5/2 times greater than for a centered rod (in the $h \ll r$ approximation). If the rod is very close (for some angles θ , the gap $\Delta r(\theta) \lesssim h\sqrt{h/r}$) to the cylinder wall additional drag is contributed by the relative motion of rod and wall.

2.2.2 Shear thickening fluids

In a shear thickening fluid the viscosity is an increasing function of the strain rate. The behavior of such fluids is complex, but

is often described as discontinuous shear thickening in which the viscosity increases abruptly by orders of magnitude if the strain rate $|\dot{\gamma}| > \dot{\gamma}_c$, where $\dot{\gamma}_c$ is a critical strain rate[2]. As a result, Eq. 2 breaks down if it implies $|\dot{\gamma}| = \frac{1}{\eta} \left| \frac{dp'}{dz} y \right| > \dot{\gamma}_c$, where η is the viscosity in the unstiffened regime. The value of $\dot{\gamma}_c$ is generally taken as an empirical parameter.

What happens if the velocity profile of Eq. 2 implies the maximum strain rate $|\dot{\gamma}|_{max} = \frac{h}{2\eta} \left| \frac{dp'}{dz} \right| > \dot{\gamma}_c$? This will first occur at the duct walls where $|\dot{\gamma}|$ is greatest. The suspension will undergo discontinuous shear thickening there. The high viscosity

of the thickened suspension makes it behave almost as a solid, narrowing the effective duct to the unstiffened region of width $h' = 2 \frac{\dot{\gamma}_c \eta}{dp'/dz}$. However, reducing h to the effective h' reduces the maximum strain rate $|\dot{\gamma}|_{max}$ so that it is below the threshold of shear thickening; this solution is not self-consistent.

The same conclusion follows if we note that the shear stress σ must be continuous across the boundary between stiffened and unstiffened regions because there is no source or sink of momentum at the boundary. That implies a strain rate $\dot{\gamma} \equiv \frac{dv}{dy} = \sigma/\eta$ orders of magnitude less in the stiffened region because η is orders of magnitude greater there. This leads to the contradiction of a strain rate $\dot{\gamma}$ greater (by a large factor) in the unstiffened region than in the stiffened region, and also explains why discontinuous shear thickening is accompanied by hysteresis[12].

A self-consistent solution is found if $|\dot{\gamma}|$ remains at the shear thickening threshold $\dot{\gamma}_c$ across the duct, aside from the central region [13]. Then, if this central region is negligibly thin, Eq. 2 is replaced by

$$v(y) = \dot{\gamma}_c \left(\frac{h}{2} - |y| \right), \quad (14)$$

$$\dot{q} = \dot{\gamma}_c \frac{h^2}{4}, \quad (15)$$

$$\dot{Q} = \dot{\gamma}_c \frac{\pi r h^2}{2} \quad (16)$$

and

$$v_{rod} = \frac{\dot{Q}}{\pi r^2} = \dot{\gamma}_c \frac{h^2}{2r}. \quad (17)$$

This result relates the shear thickening threshold $\dot{\gamma}_c$ to the measured sinking rate

v_{rod} , and is the source of the values of $\dot{\gamma}_c$ shown in the Table.

The sink rate is predicted to be independent of both the weight of the rod and the length z_{rod} of the duct between the rod and cylinder. The reason for this is that the duct dimensions are uniform along its length if the rod is parallel to the cylinder axis; if $\dot{\gamma} = \dot{\gamma}_c$ at one depth, that equality holds everywhere. The sink rate does depend on the nature of the suspension through the empirical $\dot{\gamma}_c$.

For an off-center rod the result Eq. 13 for a Newtonian fluid is replaced by

$$\dot{Q} = \int_0^{2\pi} r \dot{q}(\theta) d\theta = \dot{\gamma}_c \frac{\pi r h^2}{2} \left[1 + \frac{1}{2} \left(\frac{\Delta x}{h} \right)^2 \right]. \quad (18)$$

Then \dot{Q} and $v_{rod} = \dot{Q}/\pi r^2$ can be as much as 3/2 times greater than for a centered rod (in the $h \ll r$ approximation).

3 Results

As a test of the method and apparatus, we used a viscous Newtonian fluid, a solution of cane sugar in water. The results are shown in Fig. 3. We fit the exponent α in a relation $v_{rod} \propto t^\alpha$ to the power law portion of the data (before the rod approaches the bottom of the cylinder), finding $\alpha = -0.49 \pm 0.02$ for the steel rod and $\alpha = -0.47 \pm 0.02$ for the aluminum rod, in agreement with the predicted (Eq. 10) $\alpha = -1/2$ for a Newtonian fluid. The neglect of inertia in Eq. 9 is justified by the self-consistent result that the Reynolds number $Re = h v_{rod} / \eta \ll 1$

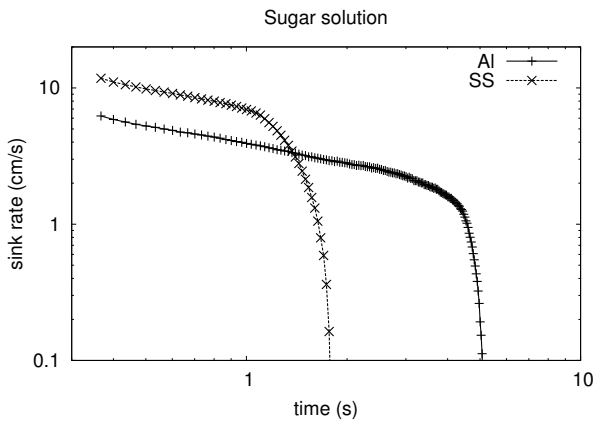


Figure 3: Sinking rate v_{rod} of aluminum and stainless steel rods in viscous cane sugar solution. From the measured sink rate and Eq. 10 the viscosity $\eta \approx 0.7$ Pa-s and the Reynolds number $Re \approx 0.1$ for the Al rod and $Re \approx 0.3$ for the steel rod at $t = 1$ s. The data sampling rate was 30/s, but the points shown represent boxcar averages of 20 points, taken to smooth otherwise noisy data.

throughout the run (at $t = 1$ s $Re \approx 0.1$ for the Al rod and $Re \approx 0.3$ for the steel rod).

The sinking rates of aluminum and stainless steel rods in suspensions of corn, potato and tapioca starches in isopycnic (density matched) CsCl brines are shown in Figs. 4–6. All suspensions had starch volume and mass fractions of 43%, well into the regime in which discontinuous shear thickening occurs, but a low enough concentration that the suspensions are shear thinning fluids (rather than pastes with finite strength) at low strain rates.

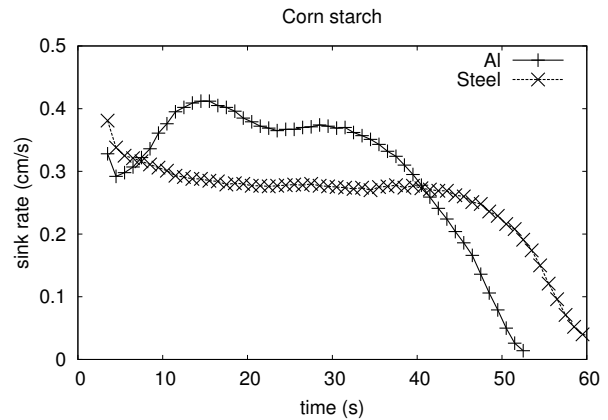


Figure 4: Sink rates of aluminum and steel rods in a 43% suspension of corn starch. Data were sampled every second, but each point shown is a boxcar average over five seconds.

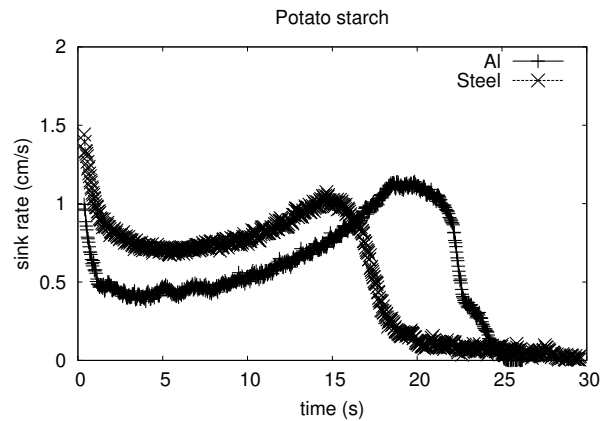


Figure 5: Sink rates of aluminum and steel rods in a 43% suspension of potato starch. The data sampling rate was 30/s, but the points shown are boxcar averages over 20 samples.

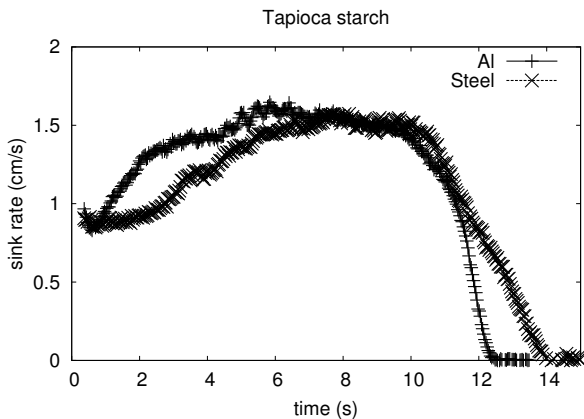


Figure 6: Sink rates of aluminum and steel rods in a 43% suspension of tapioca starch. The data were sampled at a rate of 30/s, but each point shown is a boxcar average over 20 samples.

4 Discussion

The results for the starch suspensions are mixed. In corn starch (Fig. 4) the steel rod sank at a nearly constant rate, as expected (Eq. 17) for a shear thickened suspension. The implied thickening threshold $\dot{\gamma}_c \approx 4/s$, typical of previous measurements of corn starch suspensions [2, 12, 14] (that are widely scattered, perhaps as a result of differing properties of this poorly standardized natural product). The varying sink rate of the aluminum rod might be attributed to a varying displacement from a centered position in the cylinder (Eq. 18). The greater stability of the sink rate of the steel rod was observed in two other pairs of runs (not shown).

The generally increasing sink rates in potato starch suspensions (Fig. 5) may be

attributed to motion of the rods from centered to off-center positions in the cylinder (Eq. 18). The initial decrease might be the result of a transient phase in which the suspension is unstiffened, as expected and found for a Newtonian fluid (Fig. 3). However, these are only speculations, and even the reason why corn and potato starch suspensions differ qualitatively is not understood.

In potato starch suspensions the steel rod sank about 50% faster than the aluminum rod through most of its descent, although towards the end the aluminum rod speeded up to a sink rate as fast as the maximum sink rate of the steel rod. The inferred $\dot{\gamma}_c \approx 20\text{--}30/s$.

Sink rates in tapioca starch suspensions (Fig. 6) were close to the predictions of Eq. 17: They were roughly constant after an initial increase by a factor of 1.5, consistent with motion of the rods from centered to near-wall positions (Eq. 18), and were nearly independent of the weight of the rod. This offers semi-quantitative support for the theory, but no explanation of why different starches behave so differently. The implied $\dot{\gamma}_c \approx 40/s$. We show no results for rice starch suspensions because they do not shear stiffen, unlike most other starch suspensions. We tentatively attribute this to the different shapes[15] of rice starch grains.

If the rod is initially off-center or tilted, the gap between it and the tube wall is narrower, and the shear rate greater, on one side. Shear-thickening will begin first there,

producing an upward force on that side of the immersed (lower) end of the rod. The resulting torque will tend to bring that end yet closer to the tube, increasing the misalignment and (Eq. 18) the sink rate. This is a possible, though qualitative, explanation of the increasing sink rates in Figs. 5 and 6.

This result that steel and aluminum rods behave differently was unexpected. Eq. 17 predicts not only that the sink rate should be constant until the rod nears the bottom of the cylinder, but that it should be independent of the rod's weight. The failure of this prediction indicates that there may be more to the physics than the model of Sec. 2.2.2. One possible explanation is that shear thickening depends on stress as well as on strain rate. In most rheometric experiments[2, 12] the stress and strain rate are not independently controlled, so they do not test our assumption that discontinuous shear thickening occurs of a single critical strain rate $\dot{\gamma}_c$. Our experiments, with rods of differing weights, indicate that reality is not so simple. This is an important lesson for the student—physics can be more complicated and less certain than the problems discussed in textbooks.

In one respect, the results for starch suspensions followed predictions: the sink rates were approximately independent of the rod weight, in contrast to a Newtonian fluid in which the sink rate would be proportional to the rod mass, which is three times greater for steel (and more so allowing for buoyancy).

The results are summarized in Table 1. There is no apparent correlation between the critical strain rates for discontinuous shear thickening and the size of the starch grains.

5 Conclusion

We have demonstrated a simple rheometer that can be built, or used, by students in an advanced laboratory course at slight expense and without special facilities. This rheometer can demonstrate basic but unfamiliar properties of Newtonian fluid flow as well as obtaining significant novel data about the properties of complex non-Newtonian fluids. It is suitable both as a teaching tool in a curriculum that includes hydrodynamics or rheology and as an introduction to research that produces non-trivial results without the use of expensive state-of-the-art apparatus. Students can use it to obtain quantitative data, and learn to deal with unfamiliar issues of dimensional tolerances. The most important contribution to their education may be the lesson that the behavior of real materials and experiments may not accord with theory; the empirical world is often more complicated than we can predict.

The reasons for the behavior of rods in starch suspensions shown in Figs. 4–6 and Table 1 are not understood. Possible explanations include displacement of the rods from the center of the tube, tilting, contact with the cylinder or guide sleeve, and stress dependence of the critical strain rate $\dot{\gamma}_c$. This behavior is complex enough that no simple

starch	grain diameter	$\dot{\gamma}_c$	CsCl fraction
corn	14 μ	4/s	52.5%
tapioca	14 μ	40/s	52.5%
potato	35 μ	20–30/s	54.5%

Table 1: Critical strain rates $\dot{\gamma}_c$ for suspensions of three starches in CsCl brine, inferred from the measured v_{rod} using Eq. 17. Mean grain diameters are from Snyder[15]. The mass fractions of CsCl in an isopycnic brine, used to prevent sedimentation, are also shown; we found slightly different densities for the different starches, but these values may be differ among samples of these natural products.

theory is likely to be satisfactory, and no satisfactory theory exists. This will disappoint students used to the neat derivations and explanations of textbooks (that rarely confront predictions with data, and then only in the minority of cases in which agreement is precise). However, it is an important lesson that many phenomena, even those involving everyday substances and simple experiments, are beyond the reach of theory. The research frontier begins in the undergraduate laboratory and everyday life.

Acknowledgments

This work was supported in part by American Chemical Society Petroleum Research Fund Grant #51987-ND9.

References

[1] N. J. Wagner and J. F. Brady, Shear thickening in colloidal dispersions Phys. Today 62 (10), 27–32 (2009).

[2] E. Brown and H. M. Jaeger Shear thickening in concentrated suspensions: phenomenology, mechanisms and relations to jamming Rep. Prog. Phys. 77, 046602 (2014).

[3] R. C. Stanley Non-Newtonian viscosity and some aspects of lubrication Phys. Ed. 7 (4), 193–198 (1972).

[4] A. L. Motyka An Introduction to Rheology with an Emphasis on Application to Dispersions J. Chem. Educ. 73 (4), 374–380 (1996).

[5] M. Dolz, J. Delegido, A. Casanovas and M.-J. Hernández A Low-Cost Experiment on Newtonian and Non-Newtonian Fluids J. Chem. Educ. 82 (3), 445–447 (2005).

[6] R. M. Digilov, B. Gurfinkel and M. Reiner Analysis of non-Newtonian power-law liquids with a weight-controlled capillary viscometer Am. J. Phys. 76 (10), 968–974 (2008).

- [7] R. Cross Elastic and viscous properties of Silly Putty Am. J. Phys. 80 (10), 870–875 (2012).
- [8] D. R. Dounas-Frazer, J. Lynn, A. M. Zaniewski and N. Roth Learning about non-Newtonian fluids in a student-driven classroom Phys. Teach. 51 (1), 32–34 (2013).
- [9] <http://imagej.nih.gov/ij/> accessed June 3, 2014.
- [10] W. Müller Zum Problem der Anlaufströmung einer Flüssigkeit im geraden Rohr mit Kreisring und Kreisquerschnitt Zeit. angew. Math. Mech. 16, 227–238 (1936).
- [11] G. K. Batchelor An Introduction to Fluid Dynamics (Cambridge University Press, Cambridge, 1967).
- [12] C. Chu, *et al.* Hysteresis and Lubrication in Shear Thickening of Cornstarch Suspensions Phys. Rev. E submitted (arXiv:1405.7233) (2014).
- [13] H. M. Laun, R. Bung and F. Schmidt Rheology of extremely shear thickening polymer dispersions (passively viscosity switching fluids) J. Rheol. 35 (6), 999–1035 (1991).
- [14] A. Fall, H. Huang, F. Bertrand, G. Ovarlez and D. Bonn Shear Thickening of Cornstarch Suspensions as a Reentrant Jamming Transition Phys. Rev. Lett. 100, 018301 (2008).
- [15] E. M. Snyder Industrial Microscopy of Starches, in Starch: Chemistry and Technology eds. R. L. Whistler, J. N. BeMiller and E. F. Paschall 2nd ed. 661–673 (Academic Press, Orlando, 1984).

Sum Rules in Non-relativistic Quantum Mechanics

Debnarayan Jana¹

¹Department of Physics
University of Calcutta
92 A PC Road, Kolkata- 700009, India.
djphy@caluniv.ac.in

Submitted on 28-07-2017

Abstract

In this article, we would like to discuss the implications of sum rules of non-relativistic quantum mechanics and its various forms used in atomic physics, solid state physics or nuclear physics. We also point out the connection between oscillator strength and the sum rule. As a verification of these sum rules, we will indicate their applications in harmonic oscillator and δ function potential. We would also like to indicate the apparent violation of this sum rule in rigid rotator case.

1. Introduction

Sum rules have played an important key role in the development of many branches of physics [1, 2, 3, 4, 5] such as solid state physics, atomic physics and nuclear physics since the earliest phase of quantum mechanics. This rule is important in considering the various electron transitions in solid [6]. The

sum rules have been applied in Stark effect associated with hydrogen atom [7] and in calculating the electric polarizability [8, 9].

For example, the Thomas- Reiche-Kuhn (TRK) energy-weighted sum rule [10, 11, 12]

$$\sum_k (E_k - E_n) | \langle n|x|k \rangle |^2 = \frac{\hbar^2}{2m} \quad (1)$$

was used to describe the physics of electric-dipole interactions with atoms. It was originally obtained by requiring that the Kramers-Heisenberg dispersion relation reduce to the Thomas scattering formula at high energies. A straightforward generalization of the TRK sum rule to $3d$ reads as

$$\sum_k (E_k - E_n) | \langle n|\mathbf{r}|k \rangle |^2 = \frac{3\hbar^2}{2m} \quad (2)$$

The introduction of sum rules can help students appreciate their use in research applications. The generalized TRK sum rule for dipole oscillator strengths has been established for an arbitrary atomic or molecular system [14]. In this paper, we will follow

the pedagogical approach adopted by the authors of [13] and [15].

The paper is organized as follows. In the next section, we convey the reader the simplest proof of sum rules. In section 3, we give the verification of these sum rules introduced in the earlier section. In section 4, we discuss the connection of the sum rule to oscillator strength, an important parameter used in experiment of spectroscopy. In section 5, we point out the apparent violation of sum rule in rigid rotator. In section 6, we give our conclusions.

2.Proof of Sum Rules

The derivation of non-relativistic sum rules involves the closure or completeness relation and the use of double commutator. In the proof of all the sum rules, we will follow the Heisenberg representation where the operators are time dependent while the eigenstates are not explicit function of time. The stationary energy eigenstates of a typical non-relativistic one dimensional Hamiltonian $H = \frac{p^2}{2m} + V(x)$ satisfies the discrete non-degenerate energy eigenvalue equation $H|n\rangle = E_n|n\rangle$. In this notation, the completeness can be stated as $\sum_k |k\rangle\langle k| = 1$. In case of continuous spectra, the discrete sum is replaced by the integral. For an arbitrary operator O we can write its off-

diagonal matrix elements as

$$\begin{aligned} & \sum_{all\ k} \langle n|O|k\rangle^2 \\ &= \sum_{all\ k} \langle n|O|k\rangle\langle k|O|n\rangle \\ &= \langle n|O^2|n\rangle \end{aligned} \tag{3}$$

With this basic information in quantum mechanics let us proceed to derive the first sum rule. From the fundamental commutation relation $[x, p] = i\hbar$, it is easy to note that

$$\begin{aligned} [x, H] &= \frac{i\hbar}{m}p \\ xH - Hx &= \frac{i\hbar}{m}p \end{aligned} \tag{4}$$

For a stationary state, if we take $\langle n|xH - Hx|n\rangle = \frac{i\hbar}{m}\langle n|p|n\rangle$, because of the Hermitian nature of the Hamiltonian, we conclude $\langle n|p|n\rangle = 0$. If we further consider the matrix elements of the momentum operator, then we note that

$$\begin{aligned} \langle n|p|k\rangle &= \frac{m(E_k - E_n)}{i\hbar} \langle n|x|k\rangle \\ &= \frac{m\omega_{kn}}{i} \langle n|x|k\rangle \end{aligned} \tag{5}$$

This equation (5) illustrates how one can compute the matrix elements of the momentum operator given the matrix elements of the position operator provided the discrete energy levels are known. Using the value of the double commutator $[x, [x, H]] = \frac{i\hbar}{m}[x, p] = -\frac{\hbar^2}{m}$ and the completeness relation, we note that

$$\begin{aligned} & \langle n|xxH - xHx - xHx + Hxx|n\rangle \\ &= -\frac{\hbar^2}{m} \end{aligned} \tag{6}$$

As a result, the sum rule is recovered as

$$\sum_{all\ k} (E_k - E_n) | \langle n|x|k \rangle |^2 = \frac{\hbar^2}{2m} \quad (7)$$

This equation (7) is known as the celebrated TRK sum rule. Moreover, using equation (5) and noting that

$$\langle n|p^2|n \rangle = \sum_{all\ k} \langle n|p|k \rangle \langle k|p|n \rangle \quad (8)$$

we find a relation

$$\begin{aligned} \sum_{all\ k} (E_k - E_n)^2 | \langle n|x|k \rangle |^2 \\ = \frac{\hbar^2}{m^2} \langle n|p^2|n \rangle \\ = \frac{2\hbar^2}{m} (E_n - \langle n|V|n \rangle) \end{aligned} \quad (9)$$

This equation (9) can be used to compute the expectation value of squared momentum and the potential energy. For example, the expectation value of the potential energy in the ground state of the harmonic oscillator can be easily computed as

$$\begin{aligned} \frac{2\hbar^2}{m} \langle 0|V|0 \rangle = \frac{\hbar^3\omega}{2m} \\ \langle 0|V|0 \rangle = \frac{1}{4}\hbar\omega \end{aligned} \quad (10)$$

where we have used only non-zero matrix element $\langle 0|x|1 \rangle = \sqrt{\frac{\hbar}{2m\omega}}$ in the LHS sum. As a generalization to any states $|n \rangle$, we can get the expectation value of the potential energy without invoking the wavefunction

$$\langle n|V|n \rangle = \frac{2n+1}{4}\hbar\omega \quad (11)$$

Again, noting that $[p, H] = -i\hbar\frac{\partial V}{\partial x}$ and $[p, [p, H]] = -\hbar^2\frac{\partial^2 V}{\partial x^2}$, we can derive another

important sum rule involving the second derivative of the potential energy as

$$\begin{aligned} \sum_{all\ k} (E_k - E_n)^2 | \langle n|p|k \rangle |^2 \\ = \frac{\hbar^2}{2} \left\langle n \left| \frac{\partial^2 V}{\partial x^2} \right| n \right\rangle \end{aligned} \quad (12)$$

For the special case of harmonic potential $V(x) = \frac{1}{2}m\omega^2x^2$, the above momentum squared sum rule (12) reduces to

$$\sum_{all\ k} (E_k - E_n)^2 | \langle n|p|k \rangle |^2 = \frac{1}{2}m\omega^2\hbar^2 \quad (13)$$

Futhermore, using (5), we can obtain another sum rule involving higher power of energy difference as

$$\begin{aligned} \sum_{all\ k} (E_k - E_n)^3 | \langle n|x|k \rangle |^2 \\ = \frac{\hbar^4}{2m^2} \left\langle n \left| \frac{\partial^2 V}{\partial x^2} \right| n \right\rangle \end{aligned} \quad (14)$$

The dimensionwise $\frac{\partial^2 V}{\partial x^2}$ being force \times momentum, this sum rule (14) is known as *force-momentum* one. One can verify easily the sum rule (14) for harmonic potential $V(x) = \frac{1}{2}m\omega^2x^2$ (LHS = $(\hbar\omega)^3 \times \frac{\hbar}{2m\omega} = \frac{\hbar^4\omega^2}{2m}$ while RHS is simply $\frac{\hbar^4}{2m^2} \times m\omega^2 = \frac{\hbar^4\omega^2}{2m}$).

Again noting that

$$(pH - Hp)(pH - Hp) = -\hbar^2 \left(\frac{\partial V}{\partial x} \right)^2 \quad (15)$$

and using the completeness relation, we come across another sum rule involving first

derivative of potential energy

$$\begin{aligned} & \sum_{all\ k} (E_k - E_n)^2 | \langle n | p | k \rangle |^2 \\ &= \hbar^2 \left\langle n \left| \left(\frac{\partial V}{\partial x} \right)^2 \right| n \right\rangle \end{aligned} \tag{16}$$

Since above sum rule is involved with first derivative of the potential energy, it is sometimes known as the *force squared* sum rule. Another variant of the above sum rule can be derived using (5) as

$$\begin{aligned} & \sum_{all\ k} (E_k - E_n)^4 | \langle n | x | k \rangle |^2 \\ &= \frac{\hbar^4}{m^2} \left\langle n \left| \left(\frac{\partial V}{\partial x} \right)^2 \right| n \right\rangle \end{aligned} \tag{17}$$

This sum rule also can be easily verified for harmonic oscillator potential. From RHS, we get $\frac{\hbar^4}{m^2} \times m^2 \omega^4 \times \langle n | x^2 | n \rangle$ while from LHS gives us $\frac{\hbar^5 \omega^3}{2m} (2n + 1)$. Equating these two, we conclude that

$$\langle n | x^2 | n \rangle = \frac{\hbar}{2m\omega} (2n + 1) \tag{18}$$

Another form of the above sum rule (17) is also important for calculation the expectation value used in nuclear physics and can be written as

$$\langle n | x^2 | n \rangle = \frac{m}{2\hbar^2} \sum_{all\ k} (E_k - E_n)^2 | \langle n | x^2 | k \rangle |^2 \tag{19}$$

All the above sum rules can easily generalized to higher dimensions. Another famous Bethe sum rule [16] can be derived as follows by noting the double commutation of

$[H, e^{i\mathbf{q}\cdot\mathbf{r}}, e^{-i\mathbf{q}\cdot\mathbf{r}}]$ with $H = \frac{p^2}{2m} + V(r)$ and $H|n\rangle = E_n|n\rangle$. It is easy to visualize that

$$\begin{aligned} [\mathbf{p}, e^{\pm i\mathbf{q}\cdot\mathbf{r}}] &= \pm \hbar \mathbf{q} e^{\pm i\mathbf{q}\cdot\mathbf{r}} \\ [V(r), e^{\pm i\mathbf{q}\cdot\mathbf{r}}] &= 0 \\ [H, e^{\pm i\mathbf{q}\cdot\mathbf{r}}] &= \pm \frac{\hbar}{2m} \mathbf{q} \cdot (e^{\pm i\mathbf{q}\cdot\mathbf{r}} \mathbf{p} + \mathbf{p} e^{\pm i\mathbf{q}\cdot\mathbf{r}}) \end{aligned} \tag{20}$$

Then, considering the expectation value of the n-th non-degenerate eigenstate of the both sides of the double commutator, we get

$$\begin{aligned} & \langle n | [H, e^{i\mathbf{q}\cdot\mathbf{r}}, e^{-i\mathbf{q}\cdot\mathbf{r}}] | n \rangle \\ &= \frac{\hbar^2 q^2}{2m} + \frac{\hbar}{m} \mathbf{q} \cdot \langle n | \mathbf{p} | n \rangle \\ & \sum_{all\ k} (E_k - E_n) | \langle n | e^{i\mathbf{q}\cdot\mathbf{r}} | k \rangle |^2 = \frac{\hbar^2 q^2}{2m} \end{aligned} \tag{21}$$

since the second term vanishes for stationary states. One can also derive the above sum rule(21) from the identity

$$e^A B e^{-A} = B + [A, B] + \frac{1}{2!} [A, [A, B]] + \dots \tag{22}$$

The TRK sum rule (7) follows from this sum rule in the limit $\vec{q} \rightarrow 0$.

Till now we have considered the sum rules for position or momentum operator. Are there any sum rules for the combination of the position and momentum operator? Wang [15] generalized the above sum rules by considering $F(\mathbf{r})$ ($F(\mathbf{p})$) is a well-behaved function of position (momentum).

It has been shown [15] that

$$\begin{aligned} & \sum_{all\ k} (E_k - E_0) | \langle 0 | F(\mathbf{r}) | k \rangle |^2 \\ &= \frac{\hbar^2}{2m} \langle 0 | (\nabla F) \cdot (\nabla F)^\dagger | 0 \rangle \end{aligned} \quad (23)$$

If we choose $F(\mathbf{r}) = \mathbf{r}$ ($F(\mathbf{r}) = e^{i\mathbf{q}\cdot\mathbf{r}}$) we can immediately get TRK (Bethe) sum rule. In the same spirit, equation (19) can also be derived from this generalized sum rule by assuming $F(\mathbf{r}) = r^2$. For hermitian character of $F(\mathbf{p})$, the above sum rule (23) is recast as

$$\begin{aligned} & \sum_{all\ k} (E_k - E_0) | \langle 0 | F(\mathbf{p}) | k \rangle |^2 \\ &= -\frac{1}{2} \sum_{l,n=1}^{\infty} \frac{(-i\hbar)^{l+n}}{l!n!} \\ & \left\langle 0 \left| \frac{\partial^{l+n} V}{\partial x^{l+n}} \frac{\partial^n F}{\partial p^n} \frac{\partial^l F}{\partial p^l} \right| 0 \right\rangle \end{aligned} \quad (24)$$

Choosing $F(\mathbf{p}) = p$ (only allowed values $l = 1, n = 1$) we can immediate get back the sum rule for momentum (12). Now for the combination of (x, p) , the sum rule (for hermitian operator) has been generalized [15] as

$$\begin{aligned} & \sum_{all\ k} (E_k - E_0) | \langle 0 | F(x, p) | k \rangle |^2 \\ &= \frac{\hbar^2}{2m} \left\langle 0 \left| \left(\frac{\partial V}{\partial x} \right)^2 \right| 0 \right\rangle \\ & - \frac{1}{2} \sum_{l,n=1}^{\infty} \frac{(-i\hbar)^{l+n}}{l!n!} \\ & \left\langle 0 \left| \frac{\partial^{l+n} V}{\partial x^{l+n}} \frac{\partial^n F}{\partial p^n} \frac{\partial^l F}{\partial p^l} \right| 0 \right\rangle \end{aligned} \quad (25)$$

and for non-hermitian operator, the sum

rule [15] is given by

$$\begin{aligned} & \sum_{all\ k} (E_k - E_0) | \langle 0 | F(x, p) | k \rangle |^2 \\ &= \left\langle 0 \left| \left(\frac{i\hbar}{m} \frac{\partial F}{\partial x} p + \frac{\hbar^2}{2m} \frac{\partial^2 F}{\partial x^2} \right) F^\dagger \right| 0 \right\rangle \\ & + \sum_{l=1}^{\infty} \frac{(-i\hbar)^l}{l!} \left\langle 0 \left| \frac{\partial^l V}{\partial x^l} \frac{\partial^l F}{\partial p^l} F^\dagger \right| 0 \right\rangle \end{aligned} \quad (26)$$

As practical examples of these two sum rules we consider two operators one is hermitian and other is not. The operator xp_x is not hermitian however, it can be made hermitian by choosing $Q = \frac{xp_x + p_x x}{2}$. Using (26), we find

$$\begin{aligned} & \sum_{all\ k} (E_k - E_0) | \langle 0 | xp_x | k \rangle |^2 \\ &= \frac{i\hbar}{m} \langle 0 | p_x^3 x | 0 \rangle = \hbar^3 \omega \end{aligned} \quad (27)$$

The identical result for the sum rule of Q is obtained using (25). As a second example, we consider the hermitian operator $L_z = xp_y - yp_x$ so that we can use the relation (25). Thus, the sum rule for the z-component of angular momentum of 3d harmonic oscillator [15] can be derived as

$$\begin{aligned} & \sum_{all\ k} (E_k - E_n) | \langle n | L_z | k \rangle |^2 \\ &= \frac{\hbar^2}{2m} \langle n | p_x^2 + p_y^2 | n \rangle + \\ & \frac{\hbar^2}{2} \langle n | m\omega^2 (x^2 + y^2) | n \rangle \\ &= \hbar^3 \omega (n_x + n_y + 1) \end{aligned} \quad (28)$$

where n_x and n_y are the quantum numbers of 2d harmonic oscillator. If we consider the transitions from the ground state, then the

above sum rule reduces to

$$\sum_{\text{all } k} (E_k - E_0) | \langle 0 | L_z | k \rangle |^2 = \hbar^3 \omega \quad (29)$$

Another important application of sum rule can be noticed in discussing the diamagnetic susceptibility [17] of atoms in connection with gauge transformation [18]. We know that two vector potentials resulting same magnetic field are related to each other by

$$\vec{A} = \vec{A}' + \vec{\nabla} \Lambda \quad (30)$$

The invariance of physical quantity under gauge transformation leads [18] to the following identity

$$\begin{aligned} \sum_n (E_n - E_0) | \langle n | \Lambda | 0 \rangle |^2 \\ = \frac{\hbar^2}{2m} \left(\langle 0 | (\vec{\nabla} \Lambda)^2 | 0 \rangle \right) \end{aligned} \quad (31)$$

and can be compared with equation (23). Now choosing $\lambda = xy$, we can easily obtain the sum rule

$$\begin{aligned} \sum_n (E_n - E_0) | \langle n | xy | 0 \rangle |^2 \\ = \frac{\hbar^2}{3m} \left(\langle 0 | \vec{r}^2 | 0 \rangle \right) \end{aligned} \quad (32)$$

The above equation is instrumental in deriving the negative diamagnetic susceptibility of atoms as

$$\chi = -\frac{e^2}{6mc^2} \langle 0 | \vec{r}^2 | 0 \rangle \quad (33)$$

Because of the arbitrariness of the function Λ , a variety of sum rules [19] can be obtained from equation (31).

3. Verification of sum rule in δ function potential

In this section, we would like to verify TRK sum rule in case of one-dimensional potential $V(x) = -V_0 \delta(x)$ [13]. Few things can be noted before we proceed further. This being a one-dimensional problem, there is no degeneracy associated with it. Pure dimensional analysis confirms that the binding energy $E_B \propto -\frac{mV_0^2}{\hbar^2}$. However, exact calculation demonstrates [4, 5] that there is only one bound state of magnitude $E_B = -\frac{mV_0^2}{2\hbar^2}$ and the ground state $\Psi_0 = \sqrt{\frac{mV_0}{\hbar^2}} \exp\left(-\frac{mV_0}{\hbar^2} |x|\right)$ like other quantum mechanical problem is nodeless. For the continuum states $E > 0$, the relevant wave function with free particle energy $E_k = \frac{\hbar^2 k^2}{2m}$ for non-zero dipole matrix element will be

$$\Psi_k(x) = \frac{1}{\sqrt{\pi}} \sin(kx) \quad (34)$$

A careful look into the problem indicates that there is indeed a lengthscale $a_0 = 1/K_0$ ($K_0 = \frac{mV_0}{\hbar^2}$) associated with the problem. In terms of this lengthscale, the ground state energy as well as the wave function remarkably match with those of hydrogen atom problem.

To verify the TRK sum rule (7), we have to calculate the relevant matrix element $| \langle 0 | x | k \rangle |^2$ and then perform the integration instead of discrete sum.

Using the ground state wave function

and the continuum state free particle wave function as given above, the matrix element $\langle 0|x|k \rangle$ can be computed as

$$\begin{aligned} \langle 0|x|k \rangle &= \sqrt{\frac{mV_0}{\pi\hbar^2}} \int_{-\infty}^{\infty} e^{-\frac{mV_0|x|}{\hbar^2}} x \sin(kx) dx \\ &= 4\sqrt{\frac{K_0^3}{\pi}} \frac{k}{(K_0^2 + k^2)^2} \end{aligned} \quad (35)$$

The energy difference in the sum rule is

$$E_k - E_0 = \frac{\hbar^2}{2m}(k^2 + K_0^2) \quad (36)$$

Hence, the TRK sum rule (7) can be verified as

$$\begin{aligned} \sum_{all\ k} (E_k - E_0) | \langle 0|x|k \rangle |^2 &= \int_0^{\infty} dk (E_k - E_0) | \langle 0|x|k \rangle |^2 \\ &= \frac{16\hbar^2 K_0^3}{2\pi m} \int_0^{\infty} \frac{k^2 dk}{(k^2 + K_0^2)^3} \\ &= \frac{\hbar^2}{2m} \end{aligned} \quad (37)$$

To verify the another variant of TRK sum rule (19), we need further the expectation value of $\langle 0|x^2|0 \rangle$ apart from the matrix element $| \langle 0|x|k \rangle |^2$. Using the ground state wave function, it is easy to compute the expectation value of x^2 as

$$\begin{aligned} \langle 0|x^2|0 \rangle &= \left(\frac{mV_0}{\hbar^2} \right) \int_{-\infty}^{\infty} x^2 e^{-\frac{2mV_0|x|}{\hbar^2}} dx \\ &= \frac{\hbar^4}{2m^2 V_0^2} \end{aligned} \quad (38)$$

With this expectation value, one can easily verify variant of TRK sum rule (19).

To verify the another sum rule (9), we note that

$$\begin{aligned} \langle 0|V|0 \rangle &= -\frac{mV_0^2}{\hbar^2} \\ \langle 0|p^2|0 \rangle &= \frac{m^2 V_0^2}{\hbar^2} \end{aligned} \quad (39)$$

Therefore, the RHS of the sum rule (9) is given by

$$\left(\frac{\hbar^2}{m^2} \right) \langle 0|p^2|0 \rangle = \left(\frac{\hbar^2}{m^2} \right) \times \frac{m^2 V_0^2}{\hbar^2} = V_0^2 \quad (40)$$

The LHS integral looks as

$$\begin{aligned} &= \int_0^{\infty} dk (E_k - E_0)^2 | \langle 0|x|k \rangle |^2 \\ &= \frac{4\hbar^4 K_0^3}{\pi m^2} \int_0^{\infty} \frac{k^2 dk}{(k^2 + K_0^2)^2} \\ &= V_0^2 \end{aligned} \quad (41)$$

Thus, the verification of sum rule (9) is completed. In this manner, other sum rules can be verified.

4. Oscillator Strength

The oscillator strength between two non-degenerate single electron energy states is defined as the two-thirds of the squared transition dipole moment multiplied by the energy gap between the two energy levels. Mathematically, it can be written as

$$f_{kn} = \frac{2m}{3\hbar^2} (E_k - E_n) | \langle n|\mathbf{r}|k \rangle |^2 \quad (42)$$

By its very definition, f_{kn} is a dimensionless quantity which can be easily verified from the above expression. In fact, it expresses

the probability of absorption/emission of electromagnetic (EM) radiation in associated with the transitions between energy levels of an atom or molecule. In other words, it can be thought of as the ratio between the quantum mechanical transition rate and the classical absorption/emission rate of a single electron oscillator with the same frequency as the transition. Physically speaking, it marks the number of electrons oscillating per spatial dimensions during an electronic transitions. Therefore, if \mathbf{r} contains all $3N$ spatial coordinates of N electrons, then TRK sum rule can be written in terms of oscillator strengths as

$$\sum_k f_{kn} = N \quad (43)$$

where N is the total number of electrons in the system. Hence, we notice that the sum over the oscillator strengths of all the excited states amounts to the number of electrons. Oscillator strengths are between 0 and 1. In fact, the oscillator strengths counts how much of the total oscillating potential is used for a specific transition. If there are more number of electrons available to oscillate, then naturally the transition strengths will increase. For practical purpose, the oscillator strength is usually expressed in term of frequency ν as

$$f = 1.44 \times 10^{-19} \int \epsilon(\nu) d\nu \quad (44)$$

The integral is the area under the curve of $\epsilon(\nu)$ and ν . The transition dipole strength μ is related to the oscillator strength as

$$\mu^2 = \frac{3e^2\hbar}{4\pi m\nu} \times f \quad (45)$$

In the above formula, the calculated dipole moment is expressed in cm unit. As a practical illustration of the formula, it is seen that at 800 nm, an oscillator strength of 1 corresponds to a transition dipole moment of roughly 13 Debye.

5. Sum Rule in Rigid Rotator

The sum rule in case of rigid rotator needs some attention [[20], [21]]. The rigid rotator, often regarded as a simple model of a diatomic molecule can be thought as two particles of mass m_1 and m_2 , rigidly separated at a fixed distance R . Considering the reduced mass $\mu = \frac{m_1 m_2}{m_1 + m_2}$, and its moment of inertia $I = \mu R^2$, the quantum Hamiltonian of such a system can be written as

$$H = \frac{L^2}{2\mu R^2} \quad (46)$$

where L^2 is the square of the orbital angular momentum operator depending only on angles θ and ϕ . Since $L^2|Y_{lm}(\theta, \phi)\rangle = l(l+1)\hbar^2|Y_{lm}(\theta, \phi)\rangle$, the eigenvalues of the above system is simply

$$E_l = \frac{l(l+1)\hbar^2}{2\mu R^2} \quad (47)$$

where $l = 0, 1, 2, \dots$ and the eigenfunctions $Y_{lm}(\theta, \phi)$ of the Hamiltonian are the spherical harmonics. The eigenvalues are however degenerate with respect to the azimuthal quantum number m taking values from $m = -l$ to $m = l$ including zero. Taking the polarization along the z-axis, the dipole matrix

element turns out to be

$$\langle Y_{lm} | R \cos(\theta) | Y_{00} \rangle = \frac{R}{\sqrt{3}} \delta_{l1} \delta_{m0} \quad (48)$$

As a result, TRK sum rule becomes

$$\sum_k f_{k0} = f_{10} = \frac{2\mu}{\hbar^2} \left(\frac{2\hbar^2}{2\mu R^2} \right) \frac{R^2}{3} = \frac{2}{3} \quad (49)$$

Thus, we notice an apparent violation of TRK sum rule due to the missing of additional $\frac{1}{3}$ factor to get the sum to be exactly one. This violation is due to not considering the complete Hamiltonian. In fact, the complete Hamiltonian of the above system should also include the essential part of the non-relativistic kinetic energy for the radial motion and is given by

$$H = \frac{p_r^2}{2\mu} + \frac{L^2}{2\mu R^2} + V(R) \quad (50)$$

And it is the first part of the Hamiltonian which will contribute the required $\frac{1}{3}$ factor and thus removing the apparent contradiction of TRK sum rule. However, for a perfect rigid rotator, this kinetic energy term for radial motion is absent [20] and therefore, in that case the $\frac{1}{3}$ factor will not appear.

In addition to this sum rule for dipole moment, there are also sum rules involving multipoles higher than the dipole developed essentially for nuclear transitions [22].

6. Conclusions

To conclude, we have discussed the derivation of the non-relativistic sum rules and its

various invariant forms. A connection between oscillator strength and the sum rule useful for atomic transitions has been established. The sum rules have been verified in case of harmonic oscillator and δ function potential. The apparent violation of this sum rule in rigid rotator case has also been discussed.

Acknowledgments

The author would like to acknowledge the post-graduate students for asking several interesting questions related to this subject which prompted me to write this paper. I would like to thank the anonymous reviewer for critical reading and suggestions to improve the quality of the paper.

References

- [1] R. Jackiw, *Phys. Rev.*, **157**, 1220 (1967).
- [2] H. Bethe and R. Jackiw, *Intermediate Quantum Mechanics* (2nd edition, Benjamin, NY, 1978), Chap II.
- [3] E. Merzbacher, *Quantum Mechanics*, (John Wiley and Sons, NY, 1961) pp 445-447.
- [4] R. Shankar, *Principles of Quantum Mechanics*, (Plenum, NY, 1980) p 466.
- [5] S. Gassiorowicz, *Quantum Mechanics* (2nd edition, John Wiley and Sons, NY, 1986) p 277.

- [6] S. Olszewski, *Acta Physica Polonica*, **94**, 49 (1998).
- [7] F. M. Fernandez and E. A. Castro, *Am. J. Phys.*, **53**, 757 (1985).
- [8] M. A. Maize and C. A. Burkholder, *Am. J. Phys.*, **63**, 244 (1995).
- [9] M. Traini, *Eur. J. Phys.*, **17**, 30 (1996).
- [10] W. Thomas, *Naturwissenschaften*, **13**, 627 (1925).
- [11] W. Kuhn, *Z. Phys.*, **33**, 408 (1925).
- [12] F. Reiche and W. Thomas, *Z. Phys.*, **34**, 510 (1925).
- [13] M. Belloni and R. W. Robinett, *Am. J. Phys.*, **76**, 798 (2008) and references therein.
- [14] Bing-Lu Zhou, Jiong-Ming Zhu, Zong-Chao Yan, *Phys. Rev. A*, **73**, 014501 (2006).
- [15] S. Wang, *Phys. Rev. A*, **60**, 262 (1999).
- [16] H. Bethe, *Ann. Phys.*, **5**, 325 (1930).
- [17] D. Jana, in *Astrophysics and Condensed Matter* (Horizons in World Physics, Volume 262) Edited by Thomas G. Hardwell (Nova Science Publishers, NY, USA (2008)) pp. 73-106
- [18] J. L. Friar and S. Fallieros, *Am. J. Phys.*, **49**, 847 (1981).
- [19] R. G. Sachs and N. Austern, *Phys. Rev.*, **81**, 705 (1951).
- [20] H. Hadjimechel, W. Currie and S. Fallieros, *Am. J. Phys.*, **65**, 335 (1997).
- [21] F. M. Kemandez, *Int. J. Math. Ed. Sc. Tech.*, **33**, 636 (2002).
- [22] T. J. Deal and S. Fallieros, *Phys. Rev. C*, **7**, 1709 (1973).